SPREADABILITY AND CHARACTERIZATION OF METAL POWDERS FOR ADDITIVE MANUFACTURING

A Thesis Submitted to
the Graduate School of
İzmir Institute of Technology
in Partial Fulfillment of the Requirements for the Degree of

MASTER OF SCIENCE

in Materials Science and Engineering

by
Beyza HASDEMİR

July 2020
İZMİR

ACKNOWLEDGEMENTS

I would like to express the deepest appreciation to Assoc. Prof. Dr. Çekdar Vakıf Ahmetoğlu for his guidance throughout this journey. Also, I would like to thank my co-supervisor, Asst. Prof Dr. Evren Yasa for her invaluable guidance and motivation.

I would like to express my sincere gratitude for Sentes-BIR A.S. Managing Director Çağrı Gürbüz, for his guiding comments and suggestions during my thesis.

I also thank Kenan Boz, Efe Postalcı, and Sercan Sabancı for preliminary studies in my thesis.

I would like to thank the members of our research group "Inorganic Solid Materials Group" at IZTECH.

Besides, I would like to thank Sentes-BIR R&D Center Director, Esma Ercengiz, and my colleagues who have willingly helped me during my thesis.

My second special thanks go to Fırat Mavi for his collaboration, dynamism, and friendship. Working together with him made these past months filled with laughter and new experiences. I would like to thank Laseral A.S. Director Birhan Ufku Güzel, for his permission to use Laseral MTL90 machine.

I wish to thank all of my family, especially my sister Ceyda Hasdemir for their supports.

My final and special thanks go to İbrahim Bilgiler because he's always with me.

ABSTRACT

SPREADABILITY AND CHARACTERIZATION OF METAL POWDERS FOR ADDITIVE MANUFACTURING

Powder Bed Fusion (PBF) is one of the Additive Manufacturing (AM) techniques, in which metal powders are used as feedstock. AM process enables the production of lightweight structures, design freedom in 3D printed parts, short cycle time, etc. AM made part properties are affected by the powder characteristics used to form the component. A part comprises hundreds of spread layers; however, a homogeneous layer is crucial for obtaining the necessary final part properties. Spreadability can be defined as a method to quantify the powder distribution through the layer. Although it has not been standardized yet, currently, it is merely controlled by following the powder flowability, a standardized characterization method for AM. This thesis investigates the spreadability of the utilized powders for AM (here only Laser-Powder Bed Fusion will be used), with the image processing algorithms in MATLAB. Besides, it also aims to examine the spreadability correlation with the other characteristics such as flow rate, apparent density, angle of repose, and thus the final 3D printed components. Samples in six different particle size distribution were characterized, and spreadability tests were performed with the L-PBF machine. The powder characterization results demonstrated that an increase in fine particle ratio by volume (below 20 μm) enhances the angle of repose (AOR). The tests demonstrated that irregularities on the spread layer could be quantified with the image processing algorithms. The 3D printed samples were found porous. The reason for porosity in the sample might base on a combination of various factors, poor spreadability, spatter formation, and other L-PBF processing parameters might be the reasons for such microstructural development.

ÖZET

KATMANLI İMALATA UYGUN METAL TOZLARININ YAYILIM VE KARAKTERİZASYONU

Toz Yatak Füzyon Birleştirme (PBF), hammadde olarak metal tozlarının kullanıldığı Eklemeli/Katmanlı İmalat (AM) tekniklerinden biridir. Eklemeli imalat prosesi, hafif yapıların üretimini, üç boyutlu üretilen parçalarda tasarım özgünlüğünü, kısa çevrim süresini, vb. sağlar. Eklemeli imalat ile üretilen parçanın özellikleri, parçayı oluşturmak için kullanılan toz özelliklerinden etkilenmektedir. Bir parça yüzlerce serilen katmandan oluşur; ancak, gerekli nihai parça özelliklerini elde etmek için katmanın homojenliği çok önemlidir. Serilebilirlik, katman boyunca toz dağılımını ölçmek için kullanılan bir yöntem olarak tanımlanabilir. Henüz standartlaştırılmamış olmasına rağmen, günümüzde serilebilirlik, eklemeli imalat için standartlaştırılmış bir karakterizasyon yöntemi olan toz akışkanlığını takiben kısmen kontrol edilmektedir. Bu tez, eklemeli imalat için değerlendirilen tozların (burada sadece Lazer-Toz Yatak Füzyon Birleştirme kullanılacaktır) MATLAB' deki görüntü işleme algoritmaları ile serilebilirliğini araştırmaktadır. Buna ek olarak akış hızı, sıkıştırılmış yoğunluk, yığılma açısı gibi diğer özelliklerle serilebilirlilik korelasyonunu ve dolayısıyla son üç boyutlu üretilmiş parçaları incelemeyi amaçlamaktadır. Altı farklı tane dağılımındaki toz numuneler karakterize edildi ve L-PBF makinesi tarafından serilebilirlik testleri yapıldı. Toz karakterizasyon sonuçları, hacimce ince tanecik oranındaki artışın (20 μm' nin altında), yığılma açısını (AOR) arttırdığını gösterdi. Testler ayrıca, serilen katmandaki düzensizliklerin görüntü işleme algoritmalarıyla ölçülebileceğini gösterdi. 3 boyutlu olarak üretilen numuneler gözenekli bulundu. Numunelerdeki porozitenin nedeni çeşitli faktörlerin bir kombinasyonuna dayanabilir; zayıf serilebilirlik, saçılma oluşumu ve diğer L-PBF işleme parametreleri, bu tür mikroyapısal gelişimin nedenleri olabilir.

TABLE OF CONTENTS

LIST OF FIGURES vii

LIST OF TABLES x

LIST OF ABBRAVATIONS xi

CHAPTER 1. INTRODUCTION 1

1.1. Motivation 1

CHAPTER 2. THEORETICAL BACKGROUND 4

2.1. Metal Powder Production Methods for Additive Manufacturing 4

2.1.1. Water Atomization (WA) 4

2.1.2. Gas Atomization (GA) 5

2.1.3. Plasma Atomization (PA) 7

2.1.4. Plasma Rotating Electrode Process (PREP) 7

2.2. Characterization Methods of Metal Powders for AM 9

2.2.1.Powder Morphology 10

2.2.2.Powder Flowability 10

2.2.3. Apparent and Tap Density 11

2.3.4. Angle of Repose 12

2.3.5. Particle Size Distribution 12

2.3.6. Oher Techniques 13

2.3. AM Techniques using Spherical Powders 14

2.3.1. Directed Energy Deposition (DED) 15
2.3.2. Binder Jetting (BJ) 15
2.3.3. Powder Bed Fusion (PBF) 16
2.3.3.1. Laser-Powder Bed Fusion (L-PBF) 17
2.3.3.2. Electron Beam Melting (EBM) 19
2.4. Metallic Components by PBF 20

CHAPTER 3. EXPERIMENTAL 25
3.1. Materials and Method 25
3.1.1. Materials 25
3.1.2. Equipment 25
3.1.2.1. Modification of MTL90 Machine for Spreadability Test 26
3.1.3. Development of Image Processing Algorithm 28
3.1.3.1. Preliminary Studies 28
3.1.4. Production of Cubes with L-PBF Process 31
3.2. Characterization 31

CHAPTER 4. RESULTS AND DISCUSSION 33
4.1. Powder Characterization Results of the CoCrWMo 33
4.2. Spreadability Results Determined by Image Processing 39
4.3. Porosity (%) Measurements of 3D Printed Cubes 46

CHAPTER 5. CONCLUSIONS 52

REFERENCES 53

LIST OF FIGURES

Figure **Page**

Figure 1.1. Number of published articles per year from 2010 to 2019, comparison of results from web of science with the topic keyword (a) Powder Bed Fusion of Metals (b) Metal Powder Characterization Methods for Additive Manufacturing…….3
Figure 2.1. Gas Atomization process.....……....6
Figure 2.2. Electrode Induction Melting Inert Gas Atomization …….....……6
Figure 2.3. Plasma Atomization process…….…….....7
Figure 2.4. SEM images of (a) gas atomized (b) water atomized 316L powders…….…….....10
Figure 2.5. Hall Flowmeter equipment.....……11
Figure 2.6. (a) Angle of repose (b) Apparent and (c) Tapped density..... ……12
Figure 2.7. Particle effects during powder spreading in Powder Bed Fusion process.....…13
Figure 2.8. Directed Energy Deposition process..... 15
Figure 2.9. Binder Jetting process.…....….....…..16
Figure 2.10. Basic principle of Powder Bed Fusion process (a) Computer Aided Design (CAD) file (b) Slice process (c) Layer information (d) Build process. ……...16
Figure 2.11. Solidification mechanisms in PBF process……17
Figure 2.12. Laser-Powder Bed Fusion process…….. 18
Figure 2.13. Electon Beam Melting process.....……..20
Figure 2.14. (a) optimal flowability, (b) optimal powder apparent density..... 22
Figure 3.1. The photograph of Laseral MTL90 Laser-Powder Bed Fusion machine..... ……26
Figure 3.2. Modification of Laseral MTL90 Laser-Powder Bed Fusion machine for spreadability tests. Bluetooth controller is assisted for taking the image out of building chamber.....27

Figure **Page**

Figure 3.3. Irregularities in powder-bed. Lightening is above the Inert Gas Blower 2. Irregularties precipitates, clusters, waves are shown in the image respectively.....27

Figure 3.4. Preliminary studies (a) Photographing of powder layer (platform is enclosed). (b) Homogeneous powder layer (cropped image) (c) Non-homogeneous powder layer. (d) MATLAB Image Threshold (imbinarize (K,0.3)) of non-homogeneus powder layer. (e) MATLAB Edge Detection (edge (K,'canny')) of non-homogeneous powder layer.....28

Figure 3.5. The MATLAB code used for preliminary studies…….....…….....30

Figure 3.6. Noise reduction using wiener code with different matrices in an image before MATLAB Edge Detection process (a) K = wiener2 (Groi1,[10 10]), (b) K = wiener2 (Groi1,[20 20]), (c) K = wiener2 (Groi1,[30 30]), (d) K = wiener2 (Groi1,[40 40]), (e)K=wiener2 (Groi1,[50 50]), (f) K = wiener2 (Groi1,[50 50]).....30

Figure 3.7. The 3D Drawing of the cubes on the substrate.....31

Figure 4.1. Visual examinations of the samples (a) S1, (b) S2, (c) S3, (d) S4, (e) S5, (f) S6.....33

Figure 4.2. SEM images of CoCrWMo powders in different particle size distribution. (a)(b) S1, (c)(d) S2, (e)(f) S3, (g)(h) S4, (i)(j) S5, (k)(l) S6……..….....36

Figure 4.3. The Particle size distribution (PSD) plots of the samples (a) S1 (b) S2 (c) S3 (d) S4 (e) S5 (f) S6…….....37

Figure 4.4. The angle of repose measurements of S3 and S5.....……...……..…...38

Figure 4.5. Cropped raw images of spread layers of S1 (a) layer 1 (b) layer 2 (c) layer 3. Edge detection applied layer images of S1 (d) layer 1 (e) layer 2 and (f) layer 3. Threshold applied layer images of S1 (g) layer 1 (h) layer 2 (e) layer 3…….....….....40

Figure 4.6. Cropped raw images of spread layers of S2 (a) layer 1 (b) layer 2 (c) layer 3. Edge detection applied layer images of S2 (d) layer 1 (e) layer 2 and (f) layer 3. Threshold applied layer images of S2 (g) layer 1 (h) layer 2 (e) layer 3…….....…….....41

Figure **Page**

Figure 4.7. Cropped raw images of spread layers of S3 (a) layer 1 (b) layer 2 (c) layer 3. Edge detection applied layer images of S3 (d) layer 1 (e) layer 2 and (f) layer 3. Threshold applied layer images of S3 (g) layer 1 (h) layer 2 (e) layer 3.....42
Figure 4.8. Cropped raw images of spread layers of S4 (a) layer 1 (b) layer 2 (c) layer 3. Edge detection applied layer images of S4 (d) layer 1 (e) layer 2 and (f) layer 3. Threshold applied layer images of S4 (g) layer 1 (h) layer 2 (e) layer 3.. 43
Figure 4.9. Cropped raw images of spread layers of S5 (a) layer 1 (b) layer 2 (c) layer 3. Edge detection applied layer images of S5 (d) layer 1 (e) layer 2 and (f) layer 3. Threshold applied layer images of S5 (g) layer 1 (h) layer 2 (e) layer 3…… …….....44
Figure 4.10. Cropped raw images of spread layers of S6 (a) layer 1 (b) layer 2 (c) layer 3. Edge detection applied layer images of S1 (d) layer 1 (e) layer 2 and (f) layer 3. Threshold applied layer images of S1 (g) layer 1 (h) layer 2 (e) layer 3..... 45
Figure 4.11. 3D printed cubes produced with Laser-Powder Bed Fusion Process. (a) Upper surface (f) front surface of the cubes produced by samples of S1, S2, S3 and S5 respectively. Cubes produced by (b) S1 (c) S2 (d) S3 (e) S5. Cube edge length 8 mm..... 48
Figure 4.12. The optical microscope images of the S2-1 cube on XY plane, defined points 4, 5 and 6. (scale bar: 500 μm)..... 49
Figure 4.13. The optical microscope images of the cube S2-1 on XZ plane, defined points 4, 5 and 6. (scale bar: 500 μm)..... 50

LIST OF TABLES

Table **Page**

Table 1.1. Additive Manufacturing technologies using metallic materials.....2

Table 2.1. Metal powder production methods for Additive Manufacturing.....8

Table 2.2. Metal powder characterization methods for Additive Manufacturing.....9

Table 2.3. Widely used spherical metal powders used as a feedstock.....14

Table 3.1. Chemical composition of PURESPHERE 43055 CoCrWMo.....25

Table 3.2. Laser Powder Bed Fusion process parameters on Laseral MTL90 machine…….....….31

Table 4.1. Particle size distribution (PSD) results of the samples measured with the laser diffraction method.....……..…….....……34

Table 4.2. Powder characterization results of the samples S1, S2, S3, S4, S5, S6. (- indicates no flow is obtained). Average results were given after five consistent measurements.....39

Table 4.3. Oxygen amount results of the samples measured with hot gas extraction method……..…....….….....39

Table 4.4. The average gray scale value (calculated from the cropped raw image) and black to white ratio (calculated from threshold image) of each layer after spreadability test performed by S1, S2, S3 and S5……..……..46

Table 4.5. Bulk density (g/cm^3) and Porosity (%) measurement results of the cubes……..…....….47

Table 4.6. Porosity (%) results of the cubes calculated from defined points on XY plane via image processing.....52

Table 4.7. Porosity (%) results of the cubes calculated from defined points on XZ planes via image processing…..……..….52

LIST OF ABBRAVATIONS

Additive Manufacturing	AM
Directed Energy Deposition	DED
Binder Jetting	BJ
Sheet Lamination	SL
Material Jetting	MJ
Material Extrusion	ME
Powder Bed Fusion	PBF
Electron Beam Melting	EBM
Laser Powder Bed Fusion	L-PBF
Stereolithography	.stl
Computer Aided Design	CAD
Particle Size Distribution	PSD
Angle of Repose	AOR
Scanning Electron Microscope	SEM

CHAPTER 1

INTRODUCTION

1.1. Motivation

Additive Manufacturing (AM), also known as 3D printing, is a novel production method in which materials are joined layer by layer contrary to conventional manufacturing methods. According to the F42 Committee based on AM in American Society for Testing Materials (ASTM), AM methods are categorized into seven areas: these are Material Extrusion (ME), Vat Photopolymerization (VP), Material Jetting (MJ), Sheet Lamination (SL), Powder Bed Fusion (PBF), Binder Jetting (BJ) and Directed Energy Deposition (DED).[1, 2] Three of these seven methods are metallic-based as shown in Table 1.1. Among all; PBF, BJ, and DED use spherical metal powders as a feedstock.

AM enables the production of highly complex and lightweight parts, freedom in design, without the need for joining process in short lead times, which are revolutionary novelties in Industry 4.0. AM is an important working area that involves aerospace, medical, automotive, military and biomedical industry.[3]

Metal powders are raw materials for PBF methods. Apart from this, wire and sheet form can also be used in other AM techniques. The basic working principle for powder-bed systems can be explained as follows: there is a moving platform on which a 3-dimensional structure is built. First, the blade spreads the powders to the platform before thermal energy (laser/electron beam) melts the selective regions. After the first layer is completed, the platform moves down depending on the specified layer thickness and a second layer is formed in the same fashion. The process is repeated until the complete 3-dimensional part has been finished.[3]

The homogeneity of the powders on the powder bed is crucial since a smooth thin layer is needed to provide excellent mechanical properties of the part. Homogeneity on the powder bed depends on powder properties, which are particle size, cohesive forces,

impurities, apparent/tapped density, moisture, particle shape, particle roughness, etc.[4] For instance, it is almost impossible to produce a high-density part with a powder that does not provide a good spreadability. Standard characterization methods related to powder metallurgy failed to satisfy powder properties for additive manufacturing, as they are statically analyzed with Hall flowmeter. Standard characterization methods related to powder metallurgy failed to satisfy powder properties for additive manufacturing, as they are statically analyzed with Hall flowmeter. In practical applications, the powder layer's suitability for PBF is determined by the observation of an operator or such thermal cameras as an in-situ in the 3D printing machine.

Table 1.1. Additive Manufacturing technologies using metallic materials.[5]

Process Type	**Basic Principle**	**Involved Technologies**	**Energy Source**	**Material**
Powder Bed Fusion (PBF)	Selective fusion of material in a powder bed.	Laser Powder Bed Fusion (L-PBF) Electron Beam Melting (EBM)	Laser Electron Beam	Powder
Directed Energy Deposition (DED)	Selective deposition of material to a substrate.	Laser Metal Deposition (LMD)	Laser, Electron Beam	Powder, Wire
Sheet Lamination (SL)	Fusion of stacked sheets.	Laminated Object Manufacturing (LOM) Ultrasonic Consolidation (UC)	Ultrasound	Sheet

Up to now, only few studies have suggested a solution to decrease the dependence of human control in PBF. Therefore, this thesis aims to develop a method for this shortcoming by investigating the spreadability with image processing algorithms in MATLAB and correlation between the spreadability and other existing characterization methods such as flow rate, apparent density, angle of repose of CoCrMoW powders that are produced and supplied by Sentes-BIR A.S. For this thesis, only L-PBF will be taken into consideration. As shown in Figure 1.1., the exponential growth of total published articles are illustrated with the topic keywords. According to the *web of science*, these are "Powder Bed Fusion of Metals" and "Metal Powder Characterization Methods for Additive Manufacturing."

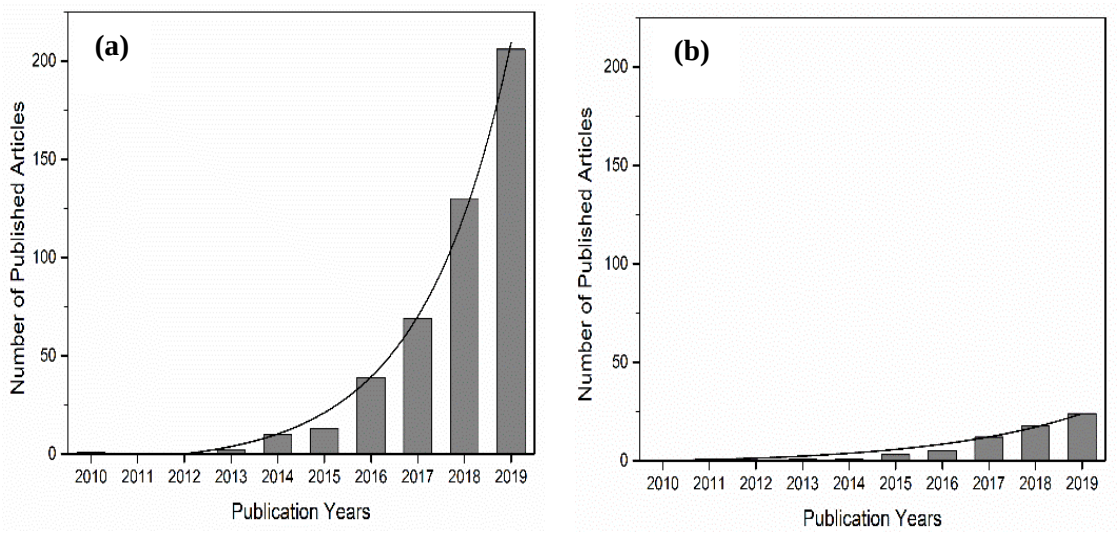

Figure 1.1. Number of published articles per year from 2010 to 2019, comparison of results from web of science with the topic keyword (a) Powder Bed Fusion of Metals (b) Metal Powder Characterization Methods for Additive Manufacturing. (Web of Science, 2020, May)

CHAPTER 2

THEORETICAL BACKGROUND

2.1. Metal Powder Production Methods for Additive Manufacturing

Metal powder production processes determine powder quality, such as PSD and particle morphology. There are many techniques for metal powder production, categorized as mechanical, chemical, and physical. However, only some of them are potential for PBF. For instance, physical methods such as gas and water atomization are widely used in powder metallurgy. Besides, novel techniques for metal powder production are plasma atomization (PA), Plasma Rotating Electrode Press (PREP), Electrode Induction Melting Inert Gas Atomization (EIGA), and Vacuum Inert Gas Atomization (VIGA). In this section, the basic principles of these methods, widely used in PBF, will be considered.

2.1.1. Water Atomization (WA)

Water atomization is the cheapest way for the production of metal powders. It is typically used for non-reactive materials. Alloy melts in an induction furnace and then pours into a small crucible fixed above the atomizer. High-pressure water is used for the scattering of the melts, and then, liquid droplets are solidified quickly in an atomization chamber. These results in the slurry include water and powder. Therefore, the drying process has become a necessity for WA. Using water for the atomization process provides high cooling rates. Besides, it decreases the solidification time of particles comparing to spherodization time. This decrease in time causes irregular particles, which include high oxygen amount produced by water atomization.[6]

2.1.2. Gas Atomization (GA)

GA is a highly common metal powder production technique for PBF. Firstly, the alloy in the ingot form melts in an induction/electric furnace. After that, the melted alloy is transferred into a tundish (small crucible). The nozzle is fixed under the tundish, and tundish connects with the atomization chamber. As the melt falls into a nozzle under the tundish, high-pressure inert gas (argon or nitrogen) is used to scatter the droplets. While scattering, the droplets are solidified and form powder particles in the atomization chamber, filled with inert gas, as shown in Figure 2.1**.** This process results in the production of spherical particles in which the particles' PSD is between 0-500 μm.[4] Copper, nickel, cobalt, aluminium, etc. alloys can be produced with gas atomization.[7]

Comparing to water atomized particles, gas atomized particles become spherical due to solidified in an inert atmosphere. Irregular particles affect the layer density and flow properties; therefore, it is not usable for PBF. [8]

The morphology of powder is related to the cooling rate during atomization. The cooling rate factors are the melting temperature of the alloy, atomization pressure, free-fall distance, and gas to metal ratio. Median particle size (dm, μm) is controlled with gas to a metal ratio (kg/kg). “K” is the constant dependent on nozzle design and material properties, “G” is the gas flow rate, and “M” is the metal flow rate shown in Equation 2.1.[9]

$$d_m = \frac{k}{\sqrt{G/M}} \qquad (2.1.)$$

Novel techniques are improved for high purity metal powders specialized in aerospace, defense, biomedical industry. These techniques are Vacuum Inert Gas Atomization (VIGA) and Electrode Induction Melting Inert Gas Atomization (EIGA). In these techniques, the melt is achieved under the vacuum. The atomization chamber installed under the furnace is entirely inert. Melting under vacuum provides degassed and refined melts. Liquid metal is atomized with high-pressure gas. The spheroidization time of particles is lower than the solidification time; thus, spherical particles can be achieved.[10]

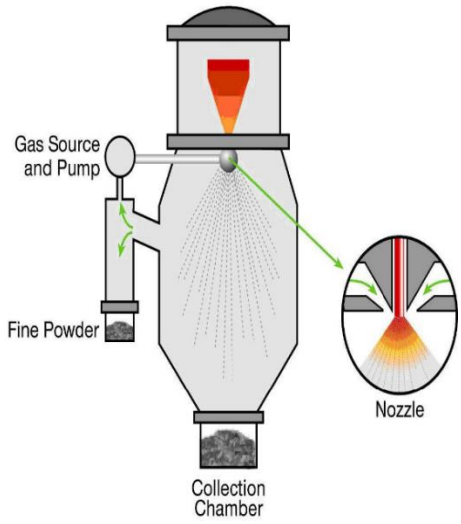

Figure 2.1. Gas Atomization process.
(Source: Dawes, 2015)[7]

For reactive metals, including low oxygen and nitrogen contents such as titanium and zirconium-based alloys, the EIGA process is required.[11] EIGA is a crucible free process, and there is no connection between melted alloy and crucible. That results in the removal of contamination, as shown in Figure 2.2. Instead of an alloyed ingot, electrodes (pre-alloyed rods) are used as a feedstock. Particles, produced by both VIGA and EIGA, do not require satellites. Besides, PSD is in the range of 0-500 μm.[12]

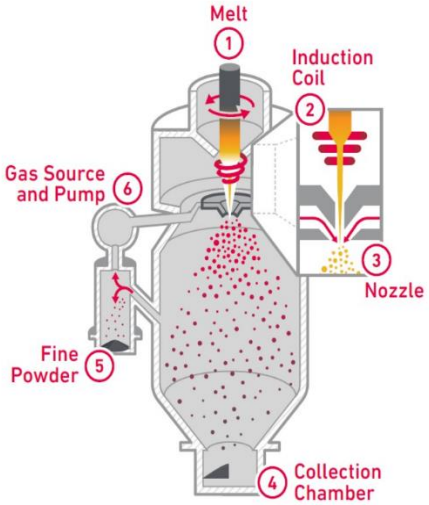

Figure 2.2. Electrode Induction Melting Inert Gas Atomization process.
(Source: web1) [13]

2.1.3. Plasma Atomization (PA)

PA is a novel method that provides the production of a high melting point and high purity spherical metal powders. A pre-alloyed wire is used as a feedstock in this method. This technique's basic working principle is as follows: first, the pre-alloyed wire is fed into an entirely inert atomization chamber and melted with a plasma torch. Then, liquid droplets are solidified in the chamber during the free-fall, as shown in Figure 2.3. Because the melting is crucible-free and takes place in an entirely inert atmosphere, it results in a low risk of contamination. The PSD range of powders produced with PA is 0-200 μm.[7]

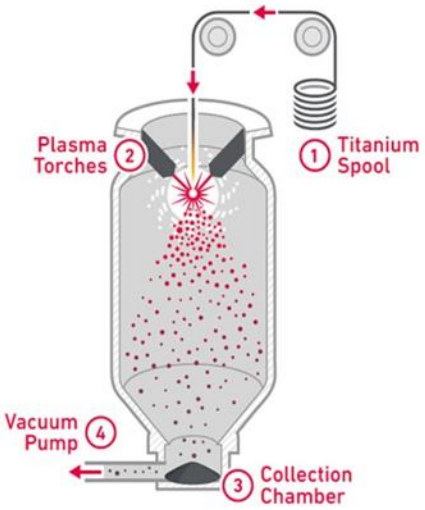

Figure 2.3. Plasma Atomization process.
(Source: web1) [13]

2.1.4. Plasma Rotating Electrode Process (PREP)

PREP is a similar metal powder production technique for plasma atomization, which is widely used in PBF. A bar of rotating electrode is used as a feedstock in PREP compared to the pre-alloyed wire used in PA. While the rotating electrode is melt through plasma torches and solidifies rapidly in the entirely inert atomization chamber.[14] Due to the entirely inert atmosphere, uncontaminated and non-oxidized highly spherical metal powders which PSD range of 0-100 μm can be produced with PREP. Titanium alloy powders can be produced with PREP.[7]

PSD of the powders, produced by PREP, highly depends on rotation speed and the diameter of the electrode bar. The mean particle size) is related to where is the empirical constant depends on the metal, is the electrode rotation speed, is the surface energy of the liquid metal, is the density of the molten metal, is the diameter of the electrode which is formulated as follows:[15]

$$D_{50} = \frac{k}{\omega}\sqrt{\frac{\gamma}{\rho D}} \qquad (2.2.)$$

Advantages, disadvantages and common uses of metal powder manufacturing methods are categorized in Table 2.1.

Table 2.1. Metal powder production methods for Additive Manufacturing. (reprinted from ref) [7]

Production Process	**Particle size, µm**	**Advantages**	**Disadvantages**	**Common uses**
Water Atomization	0-500	Range of particle sizes Only requires feedstock in ingot form	Drying required to remove water Irregular particle morphology Satellites present Low yield of powder between 20-150 µm	Non-reactive
Gas Atomization	0–500	Wide range of alloys available Suitable for reactive alloys Only requires feedstock in ingot form High throughput Range of particle sizes Use of EIGA allows for reactive powders to be processed Spherical particles	Satellites present Low yield of powder between 20–150 µm	Ni, Co, Fe, Ti (EIGA), Al
Plasma Atomization	0–200	Perfectly spherical particles	Requires feedstock to either be in wire form or powder form High cost	Ti Ti6Al4V
Plasma Rotating Electrode Process	0–100	High purity powders Perfectly spherical powder	Low productivity High cost	Ti

2.2. Characterization Methods of Metal Powders for AM

In AM, complex geometries, lightweight and high-density structures are desired. Metal powders are the feedstock of the AM. Powder properties mainly affect the part properties. Therefore, the characterization of metal powders is needed. Even though some standard characterization methods for powder metallurgy are used for additive manufacturing, those cannot adequately meet the expected properties. In 2014, the ASTM F42 committee created ASTM F3049 for the characterization of metal powders for AM. Specific powder properties are categorized as PSD, particle morphology, chemical composition, true density, and impurities content (C, S, O, N, H). Bulk powder properties are categorized as flow rate, apparent density, tap density and angle of repose.[16]

Standardized powder characterization methods are categorized in Table 2.2. Accordingly, first of all, sampling is required, then other tests should be applied for characterization. A sample ought to represent the whole batch/container. Spreadability is a significant method to detect powder layer homogeneity. Unfortunately, currently there is no standardized characterization method for spreadability. This is partially because 3D printing machine producers, market their instruments with already defined production parameters and raw metal powder sources (same for polymeric and ceramic materials). The companies impose the utilization of these parameters and powder sources to guarantee, and otherwise they do not provide any assurance of the produced part. This thesis study may open new avenues to provide more information on the utilization of outsourced powders that can be used in any available machine.

Table 2.2. Metal powder characterization methods for Additive Manufacturing.

Characterization Technique	**Standard (ASTM/ISO)**	**Characterization Technique**	**Standard (ASTM/ISO)**
Apparent Density	ASTM B212 (Hall) ASTM B417 (Carney)	**Sampling**	ASTM B215
Tap Density	ASTM B527	**Chemical Composition**	ASTM/ISO standard can be changed according to metal.
True Density by He or N Pycnometer	ASTM B923	**Static Image Analysis Method**	ISO 13322-1
PSD by Light Scattering	ASTM B822	**Dynamic Image Analysis Method**	ISO -13322-2
Sieve Analysis	ASTM B214	**Angle of Repose**	N/A
Powder Flowability	ASTM B213 (Hall) ASTM B964 (Carney)	**Spreadability**	N/A

2.2.1. Powder Morphology

Powder morphology is crucial for metal powders. It can be examined by Scanning Electron Microscope and quantified by a dynamic image analysis method. Powder morphology depends on the atomization process. Sphericity of gas or plasma atomized powders is higher than water atomized powders. SEM images of water and gas atomized 316 powders are illustrated in Figure 2. High-sphericity affects apparent/tap density, which specifies layer density for PBF.

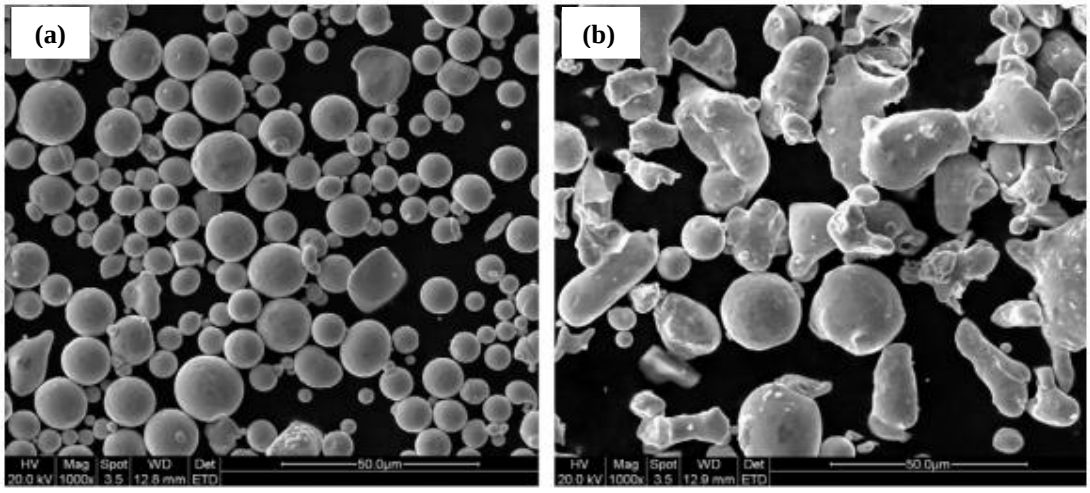

Figure 2.4. SEM images of (a) gas atomized (b) water atomized 316L powders. (Source: Li, 2010)[17]

2.2.2. Powder Flowability

A flow rate quantifies a flowability of metal powders. While the flow rate (s/50 g) of flowable metal powders is measured with Hall Flowmeter (see Figure 2.5.), non-flowable metal powders measured with Carney Flowmeter. The method works when a 50 g sample is passed through the funnel's orifice to the density cup. Through the process, time is recorded with a timekeeper. Furthermore, good flowability is a requirement for the spread of a smooth layer. Several properties affect powder flowability, and these are powder morphology, PSD, moisture, interparticle forces (Van der Walls, electrostatic forces).[16]

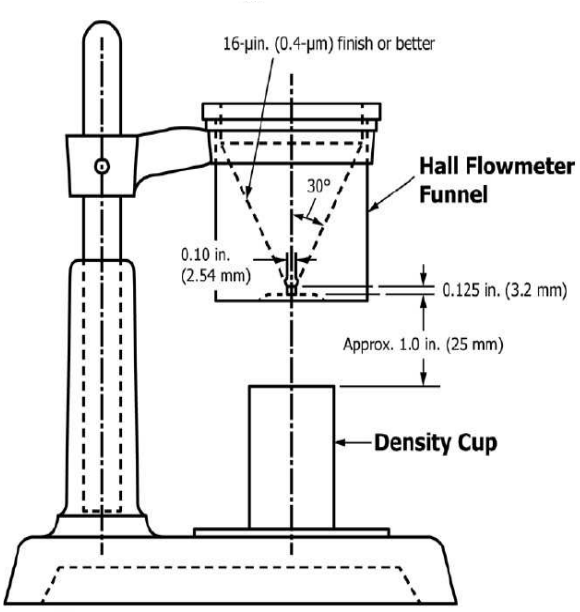

Figure 2.5. Hall Flowmeter equipment. (Source: ASTM B212)[18]

2.2.3. Apparent and Tap Density

Powder packing behavior is determined by both apparent and tap density. Like powder flowability, apparent density is measured with Hall and Carney flowmeters. A sample passes through the orifice of the funnel to the density cup, which volume is 25 cm^3. After the density cup is filled, apparent density is measured according to the contained amount. Tap density is measured with a tapping apparatus, of which tapping frequency is between 100 and 300 taps/min**.** With the effect of tapping, powder particles are packed together, a space between them decreases, as shown in Figure 2.6.b. and 2.6.c. Powder flow behavior is also quantified by the Hausner ratio (HR), which is equal to the rate of the tap density to apparent density. If the HR of the sample is higher than 1.25, it is considered as low-flowable powder.[19]

2.2.4. Angle of Repose

The angle of repose (AOR) is a characterization method for AM powders, but it has not standardized yet, according to ASTM F3049. Briefly, the AOR measures the angle of slope. However, the angle can change due to the cohesive forces and friction between the powder particles. For this method, the Hall flowmeter is used for flowable powders while the Carney flowmeter is used for non-flowable powders. As shown in Figure 2.6.a., the sample passes through the orifice of the funnel. After density cup is filled, powder particles form an angle depending on a powder flow.[8]

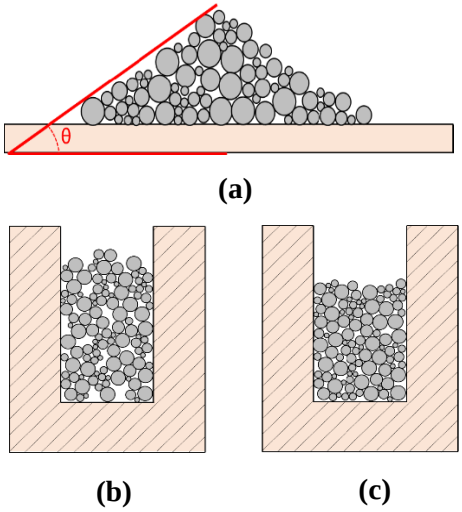

Figure 2.6. (a) Angle of repose (b) Apparent and (c) Tapped density.
(Source: Snow, 2018) [8]

2.2.5. Particle Size Distribution

In AM, different particle size distribution (PSD) can be used for each different process. Generally, for L-PBF, 15-45 µm is used, while 44-106 µm powder is used for EBM. PSD of metal powders can change depending on atomization parameters. PSD is measured with standardized laser diffraction or sieving method. Therefore, expected PSD is achieved via sieves or air classifiers. This will affect the powder flowability and layer homogeneity, which means that spreadability and apparent density during the deposition in the AM process.

2.2.6. Other Techniques

Powder spreading is a distribution of particles on the powder bed, and it is highly dynamic. Therefore, several effects occur during the spread of powder particles. These effects are illustrated schematically in Figure 2.7. Because the standardized characterization methods do not provide AM powder characteristics, recently, other characterization techniques have developed. Some of them are explained below:

- **Avalanche Angle Measurement:** This method aims to measure the avalanche angle. While the sample in the drum is rotating, a high-speed camera measures the angle from fluctuations. Because of the cohesive forces, different aspects form for different samples. Thus, flow behavior can be determined. This method mimics the AOR method.[16]
- **Shear Test with Powder Rheometer:** This method aims to measure dynamic flow and shear properties of particle friction of powders while applying torque to shear.[20]
- **Dynamic Image Analysis:** There are two kinds of image analysis methods that are static and dynamic. These methods measure both particle shape properties (convexity, sphericity, aspect ratio) and PSD. In the static method, images of particles are taken from a microscope. In the dynamic method, high-speed cameras take an image of free-flowing powder particles, and they measure the shape properties from the images.[21]

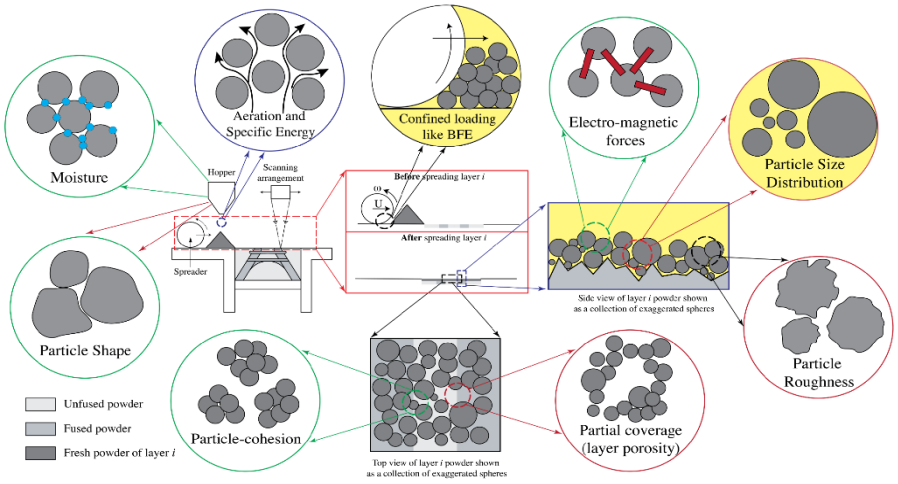

Figure 2.7. Particle effects during powder spreading in Powder Bed Fusion process. (Source: Zhang,2017).[4]

2.3. AM Techniques using Spherical Powders

Among additive manufacturing techniques, Directed Energy Deposition (DED), Binder Jetting (BJ), and Powder Bed Fusion (PBF), including Laser Powder Bed Fusion (L-PBF) and Electron Beam Melting (EBM), use spherical metal powders as a feedstock. Another categorization about these techniques can be explained as follows; DED, L-PBF, EBM are fusion-based, but BJ is non-fusion based.[45] Widely-used spherical metal powders are categorized, as shown in Table 2.3. Although this thesis is related to L-PBF, other additional techniques, using spherical metal powders, will be explained in further parts. Apart from the production technique, all these techniques require some post-processing methods such as machining, heat treatment, support and base plate removal, and surface finishing. For example, heat treatment is used for microstructure developments such as recrystallization of columnar grains transform into equiaxed grains.

Table 2.3. Widely used spherical metal powders used as a feedstock. (reprinted from ref) [22,28,29]

Base	**Alloy designation**
Fe based	18 MAR 300, 316L, 17-4PH
Ni based	Inconel 718, Inconel 725, Rene 41
Cu based	Co-Cr-Mo, Stellite 6 & 21
Ti based	Ti-6Al-4V, Ti-6Al-2Sn-4Zr-2Mo, Ti-6Al-7Nb
Al based	AlSi10Mg, AlSi7Mg, Scalmalloy
Cu based	Cu-Sn, OFHC Cu, CuNiSiCr

2.3.1. Directed Energy Deposition (DED)

DED is a fusion-based process that uses spherical metal powders as a feedstock and laser beam or electron beam as a heat source. (see Figure 2.9.) This process is not a powder-bed based like PBF; powders are deposited on the substrate layer by layer with shielding gas, which is an inert one (argon or nitrogen).[21]

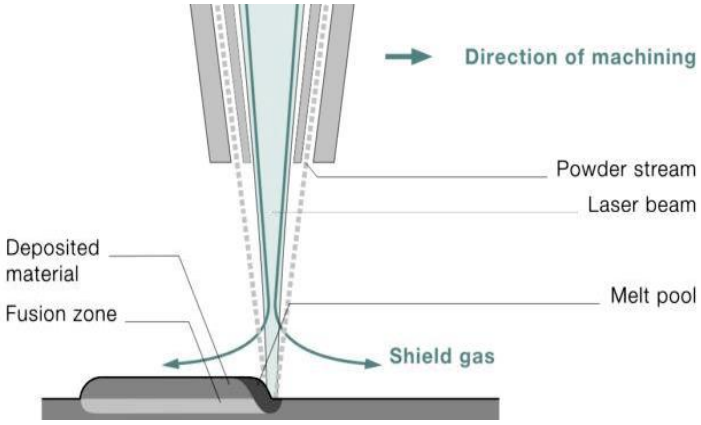

Figure 2.8. Directed Energy Deposition process.
(Source: Geyer, 2016)[23]

2.3.2. Binder Jetting (BJ)

Binder jetting is a non-fusion based process that uses spherical metal powders and polymer-based binder as a feedstock (see Figure 2.9.). This process is an alternative process for Metal Injection Molding (MIM), widely used in powder metallurgy. The process starts with CAD (Computer-Aided Design) data and then transforms into a stereolithography (.stl) file for the slicing process. The layer thickness can change according to the design of the printed part 15-300 μm. Powders spread on the build platform, and then the inkjet print head sprays the liquid binder to selective regions. The process continues until the 3D printed part is built. Because fusion is not observed, BJ requires post-processing such as curing, debinding, and sintering.[22]

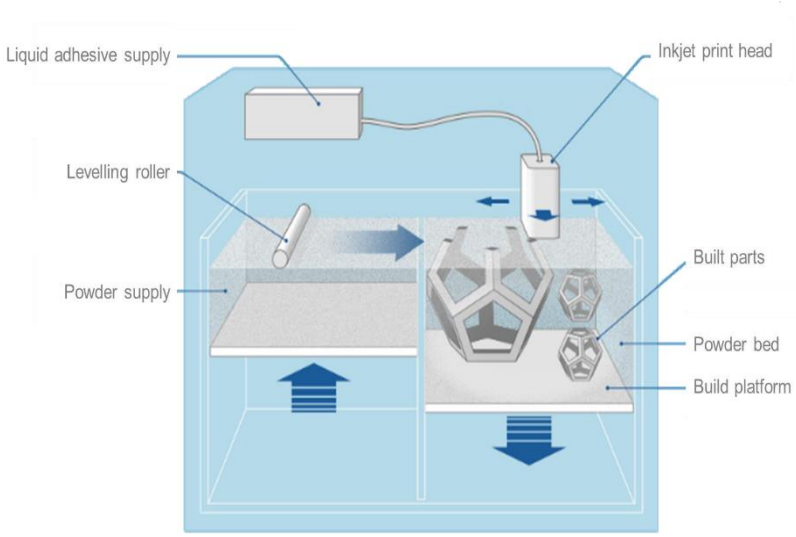

Figure 2.9. Binder Jetting process.
(Source: web3) [24]

2.3.3. Powder Bed Fusion (PBF)

PBF is one of the powder-bed based additive manufacturing methods. The process starts directly with the CAD file, like other additive manufacturing methods. Then, the CAD file is converted to the (.stl) file, which includes the triangulation of 3D design. Then, (.stl) file split up (slice process) according to specified thin layers, generally by 20-200 μm. Layer thickness can change according to the PBF process and process conditions.[25] Basic principle of PBF is shown in Figure 2.10.

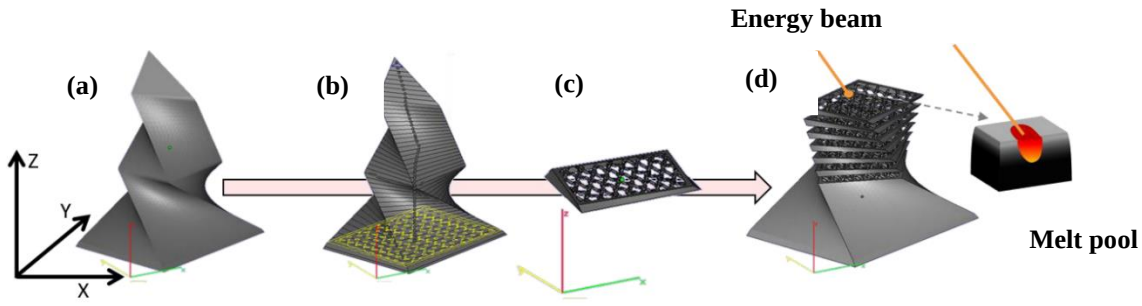

Figure 2.10. Basic principle of Powder Bed Fusion process (a) Computer Aided Design (CAD) file (b) Slice process (c) Layer information (d) Build process. (Source: Spierings, 2018)[25]

There are two main powder fusion mechanisms are full melting and partial melting. Commercial device manufacturers widely use these two methods. If the melting temperature of one of the phases in the alloy is lower than another, partial melting is formed. Recently, full-melting has started to be used for the PBF process for metals. Energy sources that are electron beam or laser for PBF melt the particles fully, and this results in the production of high-density parts, excellent bonding within layers.[10]

The powder spreading mechanism in PBF occurs with the use of a blade or a roller.[11] Thermal energy melts the selective regions on the powder bed, and melt particles fuse into the solidified layer, and this mechanism is visualized in Figure 2.11.

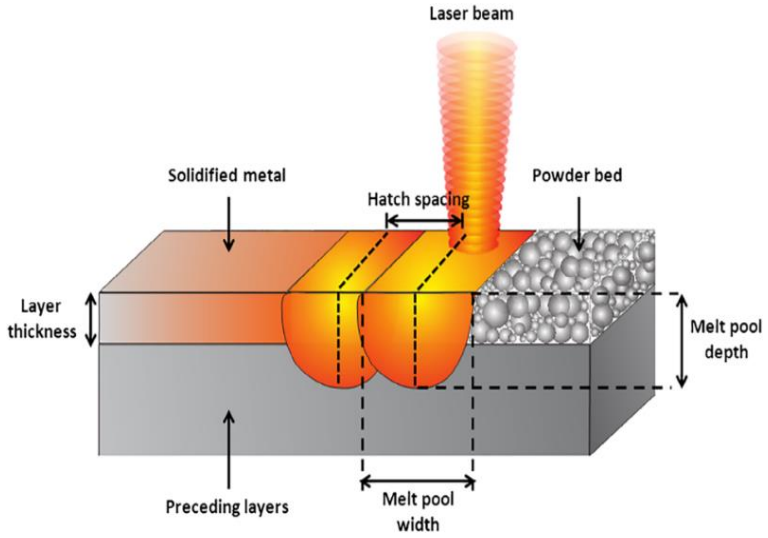

Figure 2.11. Solidification mechanisms in PBF process.
(Source: Sola, 2019)[26]

2.3.3.1. Laser-Powder Bed Fusion (L-PBF)

L-PBF process is named differently by different machine manufacturers. To give an example, EOS named the process as Direct Metal Laser Sintering (DMLS), SLM Solutions named it as Selective Laser Melting (SLM), Concept Laser named it as LaserCUSING, Renishaw named it as Metal Additive Manufacturing, TRUMPF named it as Laser Metal Fusion (LMF), 3D Systems named it as Direct Metal Printing. However, ISO/ASTM 52900 named this technology as L-PBF.

L-PBF is a layer by layer process, and the laser beam is used as a heat source that fuses the particles. The process starts with sliced stereolithography (.stl) file, and then process parameters like laser power, hatch distance, scan speed are specified for each layer. Then, the powder spreads with a blade on the build platform. Specified areas melt together, and the process continues with other layers until the geometry is finished.[3] Furthermore, the L-PBF method is shown in Figure 2.12. The typical layer thickness is 20-100 μm. Furthermore, the L-PBF method is shown in Figure 2.12. The typical layer thickness is 20-100 μm.[25] L-PBF process occurs in an inert atmosphere, in a closed chamber, and no-preheating applied on the build platform. Therefore, the solidification rate is high, specifically 10^4 -10^7 K/s. However, preheating can be applied up to 500 ºC for high melting temperature materials. That will induce the reduction of the solidification rate. Besides, N_2 or Ar can be used in an inert atmosphere depending on the reactivity of used material.[27] For instance, if the process works with Ti6Al4V, N_2 cannot be used due to the combustion reaction. Inert gas provides a decline in oxidation and contaminations. Metals and alloys used in L-PBF are Cu[28], Al[29],Fe[30], Co[31], Ti[32] and Ni[15] alloys.

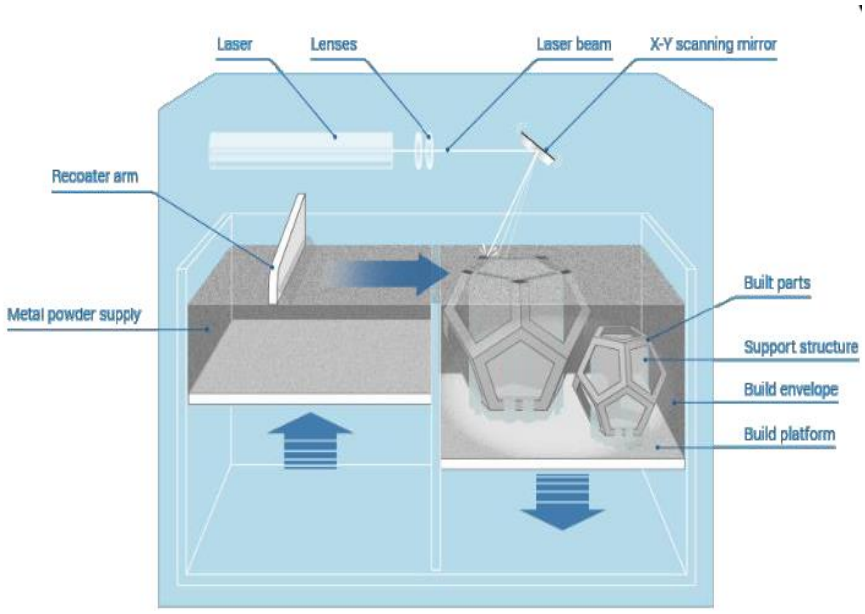

Figure 2.12. Laser-Powder Bed Fusion process.
(Source: web3) [24]

Laser power is specified according to the laser absorptivity of a material.[29] For instance, the reflectivity of copper is high comparing to nickel under the typical laser wavelength (1080 nm). Therefore, a high-power laser is used for copper. The most

common formulation (2.2.), typically used in the L-PBF process, is volumetric energy density (unit: J/mm^3) as follows; is the power of the laser (W), is the scanning speed (mm/s), is the hatch distance (mm), is the thickness of the layer (mm). These are crucial parameters for L-PBF. Hatch distance is the space between two scan lines. An increase in energy density results in effective fusing between powder particles. As a result, this causes low porosity and surface finish. Nevertheless, it increases density and mechanical properties as well.[5]

$$ED_v = \frac{P}{v\,h\,t} \tag{2.3.}$$

2.3.3.2. Electron Beam Melting (EBM)

EBM is also a layer by layer PBF process like L-PBF. As stated above, a heat source is an electron beam that fuses the particles.[5] The EBM process takes place under the vacuum. Therefore, contamination risk is lower than L-PBF. The layer thickness using in this process is 50-200 μm.[4] The electron beam is transferred via deflection and focus lens to the build platform; without this, the working principle is similar to L-PBF. The EBM method is shown in Figure 2.13. The heated build platform is used; this results in a decrease in the solidification rate. The parts produced with the EBM process are almost free from residual stresses.[8] EBM is used for conductive materials, typically metals, for electron transfer on powder particles. Some critical process parameters for EBM are; the power of the beam, the beam's focus, the beam's radius, the scanning speed of the beam, the temperature of the build platform, etc. Metals and alloys which are used in EBM are, CoCrMo (F75)[33], Inconel 718[34], Ti6Al4V[32].

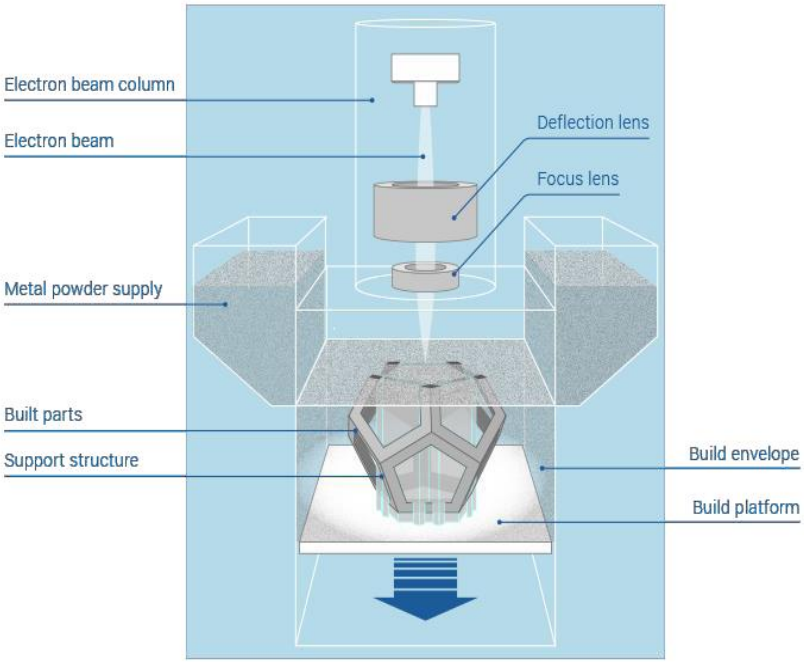

Figure 2.13. Electron Beam Melting process.
(Source: web3) [24]

2.4. Metallic Components by PBF

Up to now, researches are limited to powder spreadability in PBF. In 2015, Sun et al.[35] examined the adaption of the Ti precursor produced by the Kroll process on EBM to decrease the production costs. For adaption, they have used the Powder Manipulation Technique (PMT), a technique for Ti precursor (raw material) that is mainly higher than 250 µm. After the PMT process, particle size is principally reduced below the 150 µm. Morphology, flowability, angle of repose, apparent and tap density of PMT processed Ti powders that were in different particle size (45-106 µm, 75-106 µm, and 45-75 µm) were compared to virgin and used Ti-6Al-4V (45-106 µm) powder. As Sun et al. noted, in addition to specified process parameters, the powder feedstock's flowability also determines the spread powder homogeneity in a powder bed. They have spread the samples at the regular speed, 14 m/min, and after taking a powder bed image with an overhead camera, they observed the topography of the spread layer using MATLAB. According to their results, 45-106 µm PMT processed powder can be used for the EBM process as virgin Ti-Al-4V powder due to layer homogeneity. However, no quantitative results observed for spreadability.

In 2019, as Snow et al.[36] noted, there is no standardized method for quantifying the spreadability of metal powders that currently exist. They designed the spreadability rig and analyzed the spreadability in four metrics: the percentage of the coverage on the build plate, the rate of powder deposition, the average avalanching angle of the powder, and the rate of the change of the avalanching angle. The variables are the layer height (80μm and 40μm), recoating speed (150mm/s and 50mm/s), recoater blade material(tool steel, silicon), and powder quality gas atomized AlSi10Mg (angle of repose is 30°, 40°, and 50°). After the experiments, researchers found that powder spreadability among all metrics can be determined by the percentage of the build plate covered by powder, the rate of powder deposition, and the rate of the change of the avalanching angle. They proved that the angle of repose correlated with powder spreadability in powder-bed systems.

Brika et al.[37] were analyzed three types of Ti-6Al-4V powder, which of two plasma atomized (PSD of Powder 1: 20-53 μm, PSD of Powder 3: 15-45 μm), one of these gas atomized (PSD of Powder 2: 20-53 μm). They investigated the effect of particle size distribution and particle morphology on flowability and LPBF process (powder-bed density, mechanical properties, etc.). According to the results, Powder 2 provided better rheological behavior, high powder-bed density, and good mechanical properties due to the high sphericity. Fine particles in Powder 3 were affected by flowability in the negative cause of the cohesive forces.

In a different study, researchers noted that flowability and apparent density were directly affected by particle size distribution, the surface topology of the powder, and powder morphology in L-PBF applications.[38] Though small particles decrease the flowability for a homogenous layer, they enhance the optimal apparent density, as shown in Figure 2.14. They analyzed four different powders, widely used in additive manufacturing: Scalmalloy, Ti6Al4V, AlSi10Mg, and Inconel718. The conditioning states are as-received, air-dried, vacuum-dried, and moisturized. The effect of humidity on flowability is observed in two different spreading mechanisms: an open tool and funnel tool. According to the results, vacuum drying is a more susceptible method to prevent oxidation. Higher density alloys such as Inconel718, Ti6Al4V show higher flowability performance than low-density alloys such as AlSi10Mg and Scalmalloy. The designed tools can be used for the spreading analysis for representing the L-PBF mechanism.

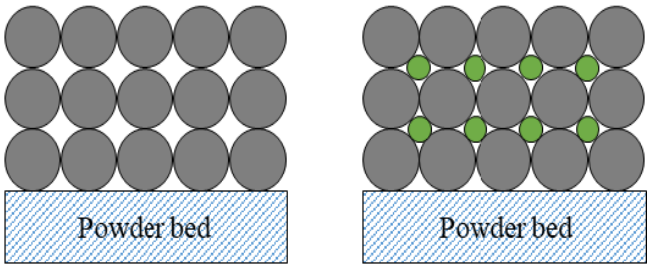

Figure 2.14. (a) optimal flowability, (b) optimal powder apparent density. (Source: Cordava, 2020)[38]

Yasa et al.[39] noted that powder particles require to be homogeneous in the layer to affect the surface roughness of the sample. According to researchers, the homogeneity in powder bed can be deteriorated by thermal stresses, coater blade scratching, and less feeding of the powders. Generally, these defects can be observed with a visual examination, but they are specified via high-speed image processing algorithms. They have used the visual camera to monitor the powder layer and determine the defects with the help of the line detection method.

There are numerous studies on powder characterization. One of them concluded that the suitability of powder for the AM process is specified by powder properties such as chemical composition, production type, density, and optical properties, as shown in Figure Figure 2.15.[40] The research team has worked on the powder flowability of nickel and iron-based powders, which are in monomodal, lognormal, and normal particle size distributions. The Flowability degree is measured visually. It is categorized by experts who are specialized in Selective Laser Melting (SLM). Then, visually categorized samples 1 to 4 (1 means very good flowability, 4 is related with insufficient flowability) are compared with powder avalanche angle, surface fractal, and particle shape quantitatively. Avalanche angle is measured with Revolution Powder Analyzer equipment that works dynamically. Like the spreading process in PBF, the powder is rotated in a rotating drum, and the camera takes the images of fluctuations consistently. According to results, samples involving agglomerations are categorized as higher than 2.5. In this rate, the avalanche angle is higher than 50^{o} for nickel-based and 45^{o} for iron-based powders. The flowability of powders in monomodal PSD is lower than powders in bimodal PSD. Visual categorization is correlated with quantitative methods, but they do

not correlate with powder spreadability during spreading in the L-PBF process. Apart from those researches, there are also studies about powder characterization.[41, 42]

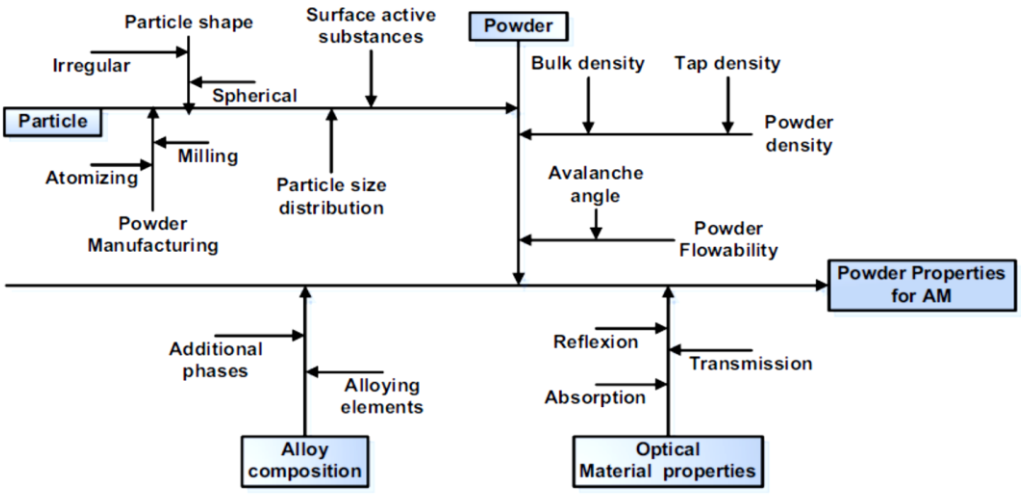

Figure 2.15. Layer properties depends on powder properties for additive manufacturing. (Source: Spierings, 2016) [40]

In another study, researchers noted that humidity, roughness on the particle surface, and chemical composition affect the flowability, even if PSD and particle shape of the powders affect the powder flowability.[43] They have used gas atomized Ti-45Nb, Ti-23Nb-10Zr, and NiTi powders and plasma atomized Ti-6Al-4V, which are in different particle sizes (25-45 µm and 45-100 µm). They compared them with rheological properties: cohesive index, angle of repose, heap height tapped density, and bulk density. GranuDrum equipment has been used for cohesive index measurement. According to the results, samples in which particle size is 45-100 µm have good flowability due to the low cohesive index. Smaller particles and irregular-shaped particles increase the cohesive index due to the effect of cohesive forces and results in poor flow. Although the particle size of the reference powder is lower than 45 µm, it shows good flowability because its morphology is more spherical due to the plasma atomization method.

In addition to powder characterization studies, some researchers also employed experiments and observed the effect of powder properties on part properties. In 2011, Spierings et al. have worked on three gas atomized 316L powders (Type I, Type II, and Type III). They examined the effect of PSD on surface quality, density, and mechanical

properties of the part.[44] Among them, PSD of Type I is a small range (7.12-24.17 μm), Type II (19.84-41.13 μm), and Type III (15.26-55.54 μm) is a coarser range. They have worked on SLM with two different layer thicknesses, 30 and 45 μm, and three orientation, 0^o, 45^o, and 90^o. They found that the interaction of laser and powder can cause sputtering and, particle size distribution can change during the process in powder-bed systems. According to their results, the lowest surface roughness is given by Type I, and higher surface roughness is given by both Type II and Type III due to layer density. They investigate the porosities of the parts with SEM. They found that the sizes of pores are larger in Type III (length of the pores below 100 μm) than Type I (the length of the pores is below 50 μm). Since big particles (between 45-55 μm) provide an effective powder layer, they cause the porosities. (if it does not include fine particles below 15 μm).

Recently, computational modeling studies have begun in addition to experimental studies for spreadability. In 2019, Chen et al. have used the Discrete Element Method (DEM) simulation at the particle level to determine the packing density of the powder layer for the powder-spreading process.[45] They stated that the density of the powder layer provides effective fusion, and it reduces the failures in the produced parts such as porosity. Nine different particle sized 316L powders, divided into three groups (range of group 1 is 53-96 μm, group 2 is 0-62 μm, and the group is 11.6- 56.2 μm) are used. 15x15 mm^2 sintered samples are simulated with DEM simulation to determine the effect of particle size on spreadability. As a result of this research, they concluded that the packing density of small particle sized powders is low due to the agglomerations of cohesive forces. Bimodal powders, including small and coarse particles, might cause segregation and voids in the powder layer. Other studies did similar simulations about powder spreadability; Nan et al.[46], Meier et al.[47], Ahmed et al.[48] have also modelled spreadability with using DEM simulations.

CHAPTER 3

EXPERIMENTAL

3.1. Materials and Method

3.1.1. Materials

PURESPHERE 43055 CoCrWMo metal powder was used in the experiments, especially in dental applications such as dental crowns, bridges for commercial purposes. The production method of the powder is gas atomization, and the morphology is spherical. Sentes-BIR A.S. produced and provided the material. Table 3.1. illustrates the chemical composition of the powder, which measured by ICP-OES. Six different samples named as S1, S2, S3, S4, S5, S6 were used with different particle sizes. Samples were prepared by sieving according to specified particle sizes. Retsch Sieve Shaker (Model No: AS200 Basic) equipment and 20 µm, 38 µm, 45 µm, and 63 µm sieves were used.

Table 3.1. Chemical composition of PURESPHERE 43055 CoCrWMo.

Element (wt.%)	Mn	W	Cr	Mo	Si	Fe	Co
PURESPHERE 43055	0.08	5.40	26.82	4.66	0.90	-	Balance

3.1.2. Equipment

The Laseral MTL90 L-PBF machine was used for the experiments. This machine is designed especially for dental applications, including dental restorations (crowns, bridges), and it uses metal powders as a feedstock. The laser type is Yt-fiber laser (200 W, wavelength of 1064 nm), building platform is circular, and the volume is ∅ 90 mm x 35 mm, the oxygen content is limited to 0.1 wt.%. Besides, the build chamber environment is pure nitrogen (%99.99) for protection from oxidation. The photograph of Laseral MTL90 machine is shown in Figure 3.1.

Figure 3.1. The photograph of Laseral MTL90 Laser-Powder Bed Fusion machine.

3.1.2.1. Modification of MTL90 Machine for Spreadability Test

For spreadability tests, taking each layer's image is needed to observe powder particle behaviors during spreading. Therefore, the spreading system of Laseral MTL90 was modified to take layer images. The photographing apparatus is designed for this purpose. The apparatus has four legs, and the material is stainless steel, the height is 430 mm, width is 90 mm, and the length is 430 mm. The hole in which the diameter is 6 mm, was drilled to place the cell phone camera (Model No: iPhone 6). The blade material is rubber, and ∅ 30 mm building platform was used. For the lighting, white LEDs were bonded to black cardboard. The cellphone and photographing apparatus were fixed because all images had to be taken from the same fixed point before image processing. For detecting the right light location, images were taken from both x-direction and y-direction of the build platform, and above the inert gas Blower 1 and inert gas Blower 2. The position of light above the inert gas blower provides a clear vision of the powder-bed irregularities. The apparatus is shown in Figure 3.2. and the possible errors in the powder bed are shown in Figure 3.3.

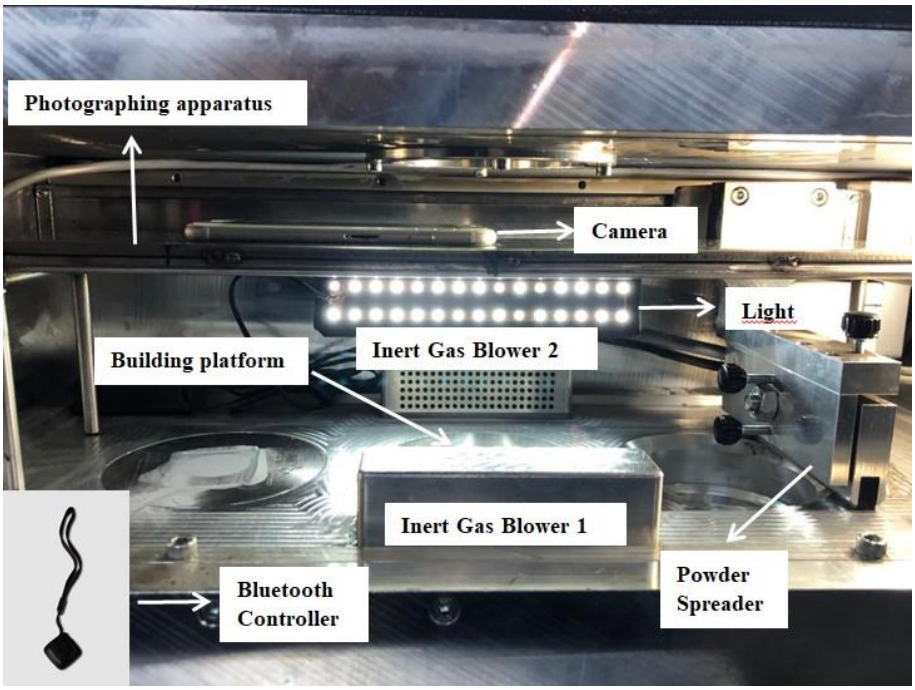

Figure 3.2. Modification of Laseral MTL90 Laser-Powder Bed Fusion machine for spreadability tests. Bluetooth controller is assisted for taking the image out of building chamber.

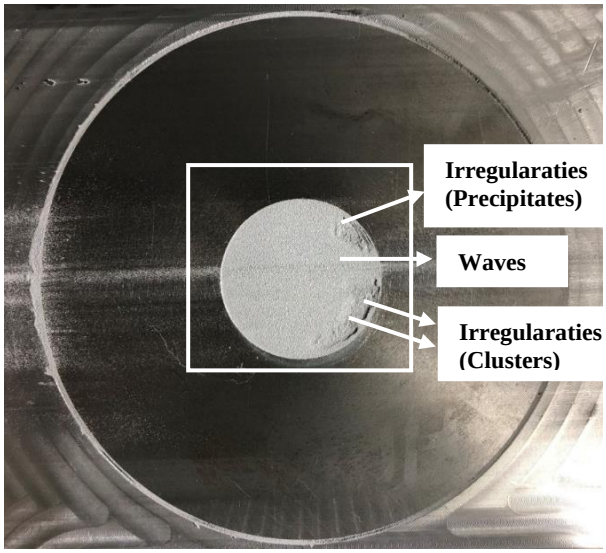

Figure 3.3. Irregularities in powder-bed. Lightening is above the Inert Gas Blower 2. Irregularties precipitates, clusters, waves are shown in the image respectively.

3.1.3. Development of Image Processing Algorithm

3.1.3.1. Preliminary Studies

To be able to detect the spreadability behavior of the samples, which are in different PSD, MATLAB image processing algorithms were used. On preliminary studies, a powder sample was filled to the platform homogeneously and non-homogeneously (with a drawing a line approximately 1 mm). Then, the image is taken above the platform, and the flash is positioned on x-direction. The thickness of the layer is about 1 mm. For the tests, the nickel-based metal powder was used. This preliminary study aims to observe irregularities on the powder bed and examine whether they were detected. MATLAB Threshold and MATLAB Edge Detection were used. These steps are shown in Figure 3.4. respectively.

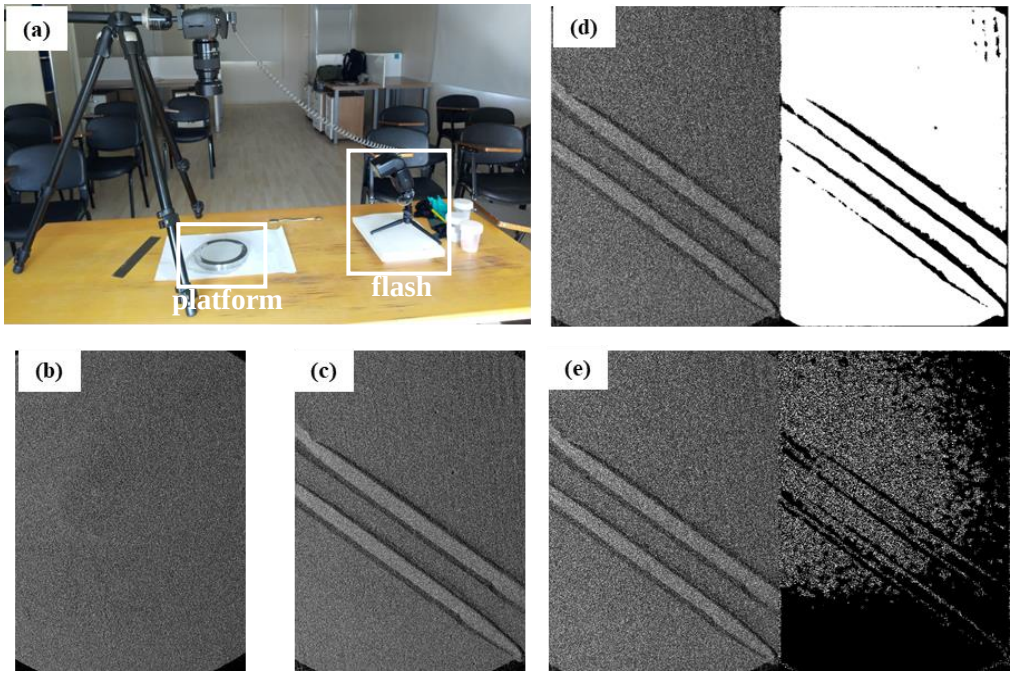

Figure 3.4. Preliminary studies (a) Photographing of powder layer (platform is enclosed). (b) Homogeneous powder layer (cropped image) (c) Non-homogeneous powder layer. (d) MATLAB Image Threshold (imbinarize (K,0.3)) of non-homogeneus powder layer. (e) MATLAB Edge Detection (edge (K,'canny')) of non-homogeneous powder layer.

Other trials were applied to images taken after modification of the Laseral MTL90 Laser-Powder Bed Fusion machine for spreadability tests. Edge detection and image threshold algorithms tried on the cropped image, which is shown in Figure 3.3. Before specifying the steps of code, the fundamental principle of image processing can be expressed as follows. The pixel, the smallest unit of the image that forms the photograph, consists of small dots, which can be seen with image processing programs. These small dots represent the value of the photographic light, consisting of black and white, which express the darkest and brightest values that form the photograph. The value expressed as 0 specifies black, while 255 specifies white. Every pixel has a three-color code, expressed as red, green, blue (RGB) value. RGB value is between 0 and 255 for each image. The code used for preliminary studies is shown in Figure 3.5. The first row provides access to the file; roi indicates a region of interest. The second row provides read the image. The third row provides the transform of RGB to grayscale. Wiener code works for noise reduction in an image. So that, different matrices which are [10 10], [20 20], [30 30], [40 40], [50 50] were tried for noise reduction as shown in the Figure 3.5. b, c, d, e, f, respectively. Then, [40 40] matrix was chosen as a suitable. Imbinarize code works for creating a threshold from a grayscaled image. The threshold value between 0 and 1, 0.5 was chosen as suitable. Canny is a function used for edge detection in the image processing algorithm.

```
roi1_filename=['C:\image.jpg'];
roi1=imread(roi1_filename);
Groi1=rgb2gray(roi1);
K = wiener2(Groi1,[40 40]);
BW1 = imbinarize(K, 0.5) ;
BW2 = edge(K, 'canny');
```

Figure 3.5. The MATLAB code used for preliminary studies.

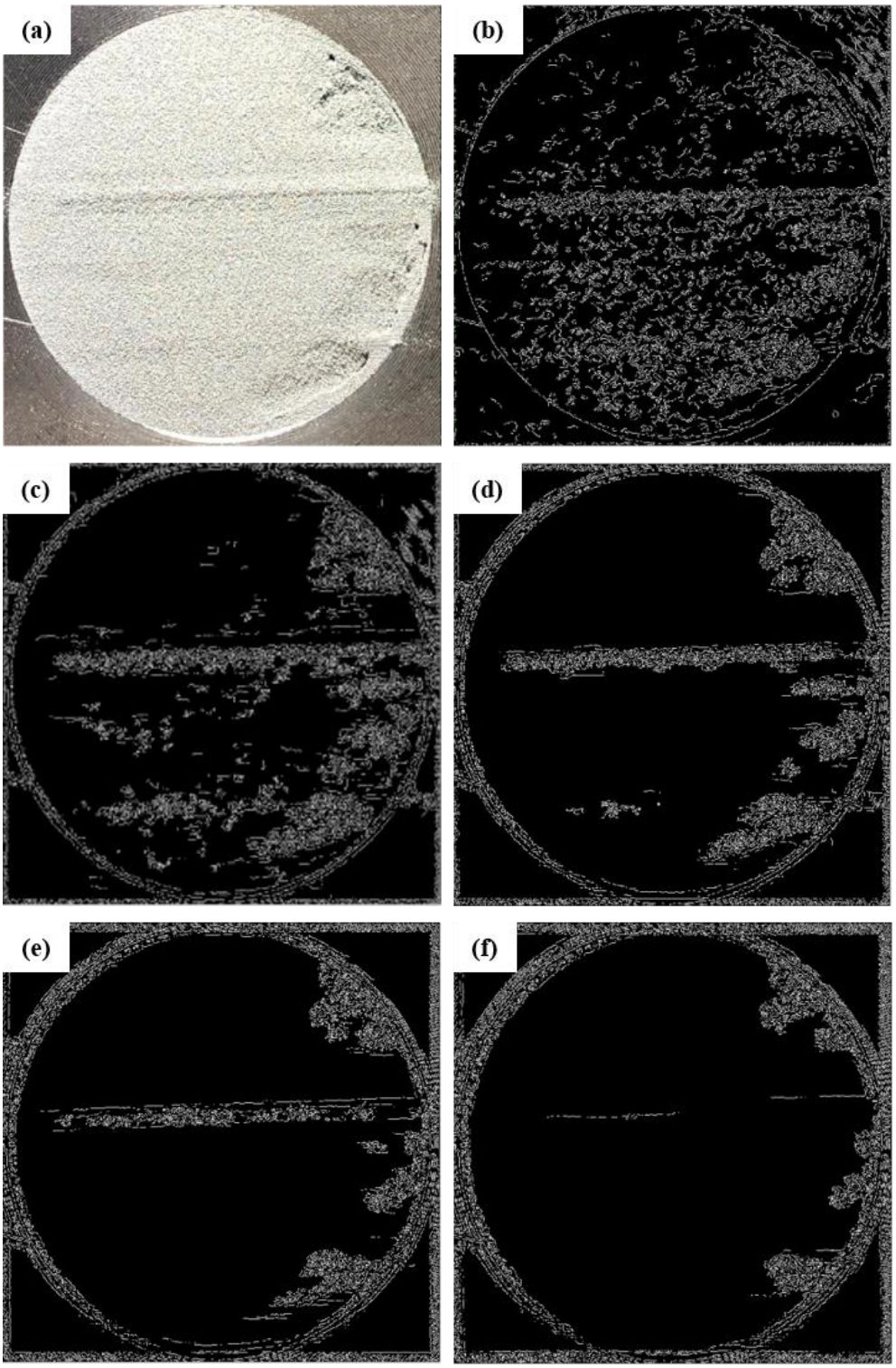

Figure 3.6. Noise reduction using wiener code with different matrices in an image before MATLAB Edge Detection process (a) K = wiener2 (Groi1,[10 10]), (b) K = wiener2 (Groi1,[20 20]), (c) K = wiener2 (Groi1,[30 30]), (d) K = wiener2 (Groi1,[40 40]), (e)K=wiener2 (Groi1,[50 50]), (f) K = wiener2 (Groi1,[50 50]).

3.1.4. Production of Cubes with L-PBF Process

Cubes were produced by the L-PBF process with the Laseral MTL90 machine. During the experiment, four different samples were used. Samples were determined according to particle size. Process parameters are given in Table 3.2., and 3D drawings of the cubes are shown in Figure 3.6. The nitrogen gas was used for the inert atmosphere, and the oxygen amount was 0.1 ppm on the chamber. After production, porosity (%) of the cubes were characterized by three different methods.

Table 3.2. Laser Powder Bed Fusion process parameters on Laseral MTL90 machine.

Laser Power	Layer Thickness	Hatch Distance	Scanning Speed	Orientation
160 W	50 µm	50 µm	400 mm/s	0º, 90º

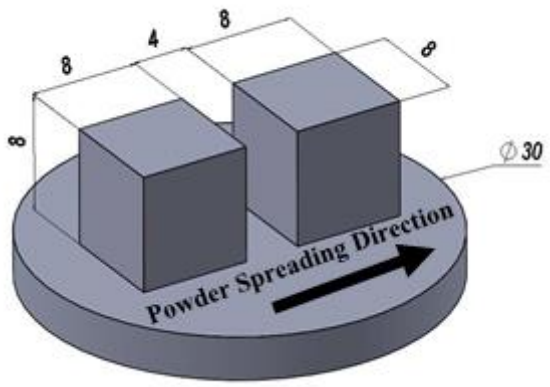

Figure 3.7. The 3D Drawing of the cubes on the substrate.

3.2. Characterization

Cubes were produced by the L-PBF process with the Laseral MTL90 machine. DuriThe morphological characterization of PURESPHERE 43055 CoCrWMo powders, which in different PSD, were analyzed by Scanning Electron Microscopy (SEM; Thermo Scientific Apreo S). The samples' particle size was measured by Laser Diffraction Analysis (Malvern Panalytical Mastersizer 2000) and measured from SEM images by using the Image J program. Flow rate, apparent density, and angle of repose

measurements were conducted by Hall flowmeter (produced according to ASTM B212 standard by Sentes-BIR. Tapped density measurement was performed by Tapped Density instrument (produced according to ASTM B527 standard by Sentes-BIR). The angle of repose measurements was conducted with Hall flowmeter and marking gauge. The alloy's chemical composition was measured by Inductively Coupled Plasma Emission Spectroscopy (Perkin Elmer Avio 200). The oxygen amount is measured with an inert gas fusion principle (Leco TC400 instrument). Density measurements were conducted by using geometric measurements (caliper, Precisa XB220A precision balance), Archimedes method (Precisa XB220A Archimedes kit), and image processing method (Nikon Eclipse LV150N; NIS Elements BR). Bulk density measurements were conducted according to the ASTM B962-17 standard. Used AccuPyc II conducted the true density of the powder according to the ASTM B923-16 standard.

CHAPTER 4

RESULTS AND DISCUSSION

4.1. Powder Characterization Results of the CoCrWMo

CoCrWMo powder samples, coded as S1, S2, S3, S4, S5, S6 were prepared with sieving in different sized mesh sizes. The sieving procedure of the samples was specified to determine the effect of powder properties on spreadability behaviors. For instance, S6 was chosen to verify the spreadability behavior of S3. S1 and S4 were chosen to observe the effect of fine particles on spreadability behavior.

Visual examination of samples after sieving was shown in Figure 4.1. According to visual examinations, S1, S2, S3, and S6 seemed flowable, while S4 and S5 seemed non-flowable due to the agglomerated particles.

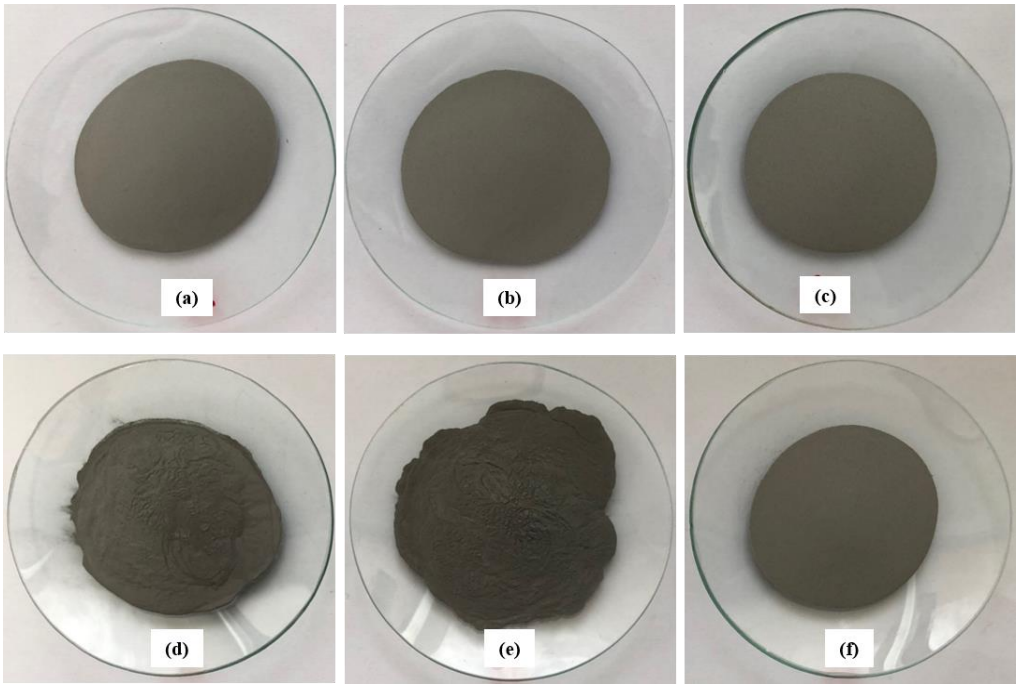

Figure 4.1. Visual examinations of the samples (a) S1, (b) S2, (c) S3, (d) S4, (e) S5, (f) S6.

Particle size distribution (PSD) of the powder samples was analyzed with the laser diffraction method. Also, size measurements of the particles were measured using the Image J program from SEM images to support the laser diffraction analysis results. While the D_{10}, D_{50}, and D_{90} values of the S1 and S2 are similar to each other, differences in particles are below 20 µm and higher than 45 µm. That may cause different spreadability behaviors. Besides, D_{10}, D_{50}, and D_{90} values of the S3 and S6 are almost similar, but the S3 includes coarser particles higher in volume. S5 is a sample that involves the highest fine particles, a ratio of particles below 20 µm is 66.58 percent, which causes poor flowability. Also, S4 includes fine particles, and the ratio of particles below 20 µm is 54.85 percent.

Table 4.1. Particle size distribution (PSD) results of the samples measured with the laser diffraction method. (Average results were given after three consistent measurements.)

Sample Name	**S1**	**S2**	**S3**	**S4**	**S5**	**S6**
D_{10} (µm)	17.13	20.07	36.58	8.16	0.25	33.33
D_{50} (µm)	27.71	32.02	49.92	18.26	14.94	45.20
D_{90} (µm)	44.18	50.00	67.90	44.12	34.56	61.17
≤ 10 µm (%)	0	0	0	18.26	28.06	0
≤ 20 µm (%)	19.66	9.82	0	54.85	66.58	23.42
20 µm-38 µm (%)	60.37	58.21	13	29.87	26.13	25.86
38 µm-45µm (%)	10.91	14.98	20.42	5.90	3.78	25.30
45 µm-53 µm (%)	6.17	9.97	26.34	4.43	2.40	17.25
53 µm-63 µm (%)	2.65	5.55	23.41	3.16	1.11	7.20
63 µm-75 µm (%)	0.24	1.47	13.02	1.57	0	0.97
75 µm-90 µm (%)	0	0	3.56	0.22	0	0
90 µm-106 µm (%)	0	0	0.25	0	0	0
106 µm -125 µm (%)	0	0	0	0	0	0

The morphology of the powder samples in six different particle size distribution was analyzed qualitatively by SEM. The morphology of the samples is highly spherical, but some samples can include irregular particles, as shown in Figure 4.2. The reason for the spherical or irregular shapes of the particles can be explained with gas atomization process parameters. Two images were taken from each sample at 1000X and 2000X magnifications. Besides, size measurements of particles were measured by using the Image J program from SEM images.[49] The data (diameter of the circle) obtained by Image J measurements is two dimensional. Stereological equation $D_{sphere} = D_{circle}/0.785$ was applied to convert 2D measurements to 3D values. [49,50]

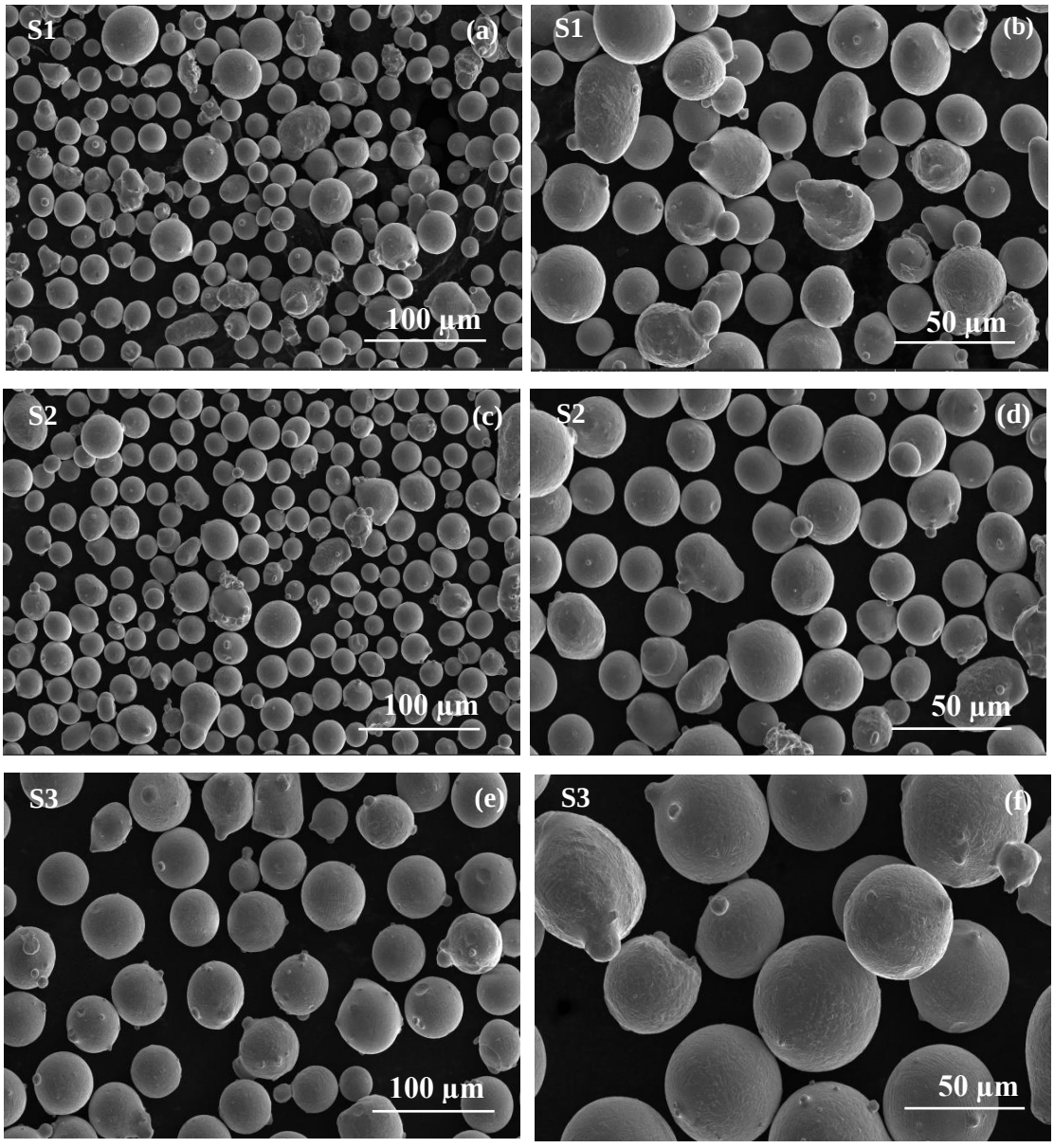

(Figure 4.2. is continued on next page)

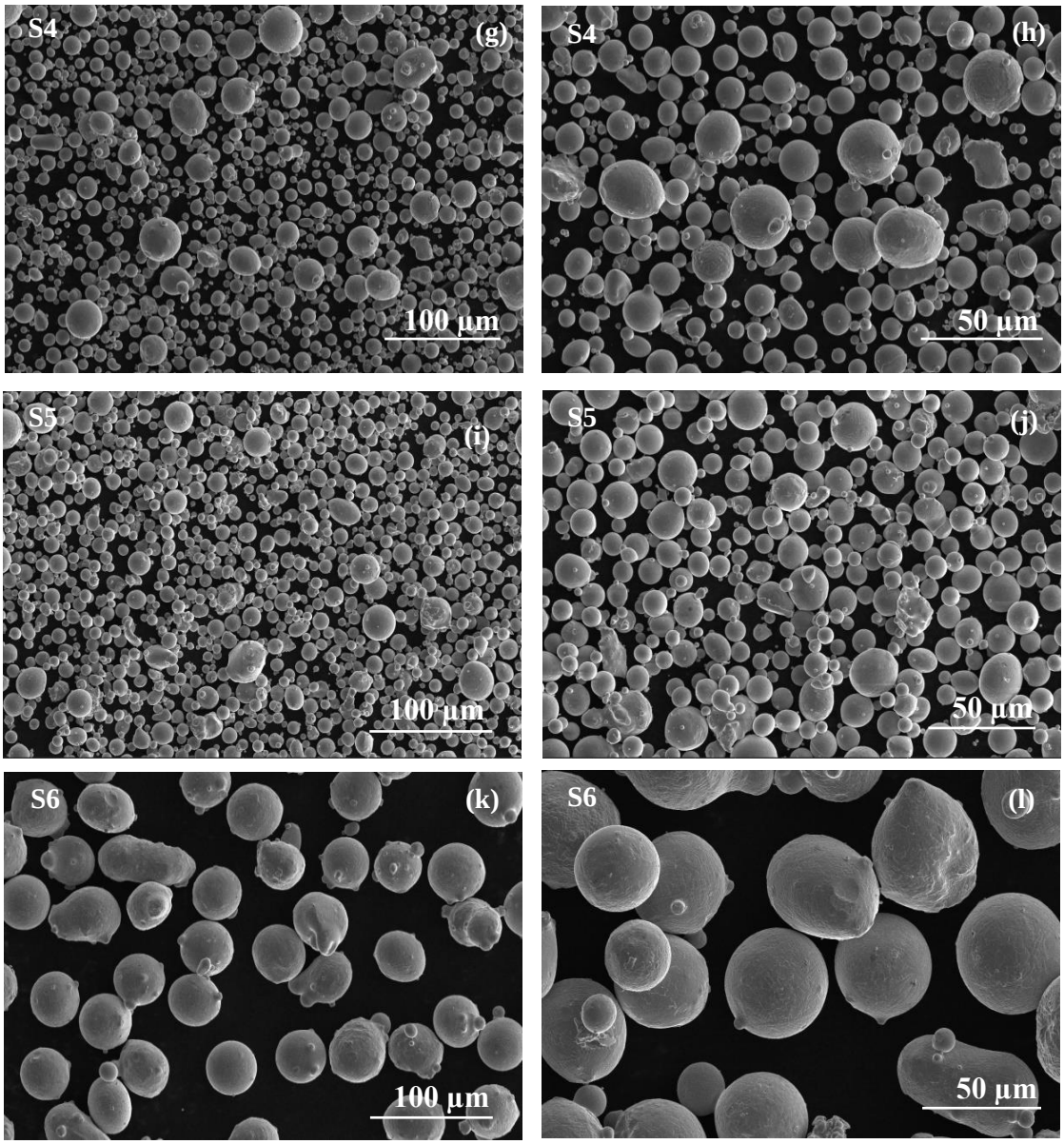

Figure 4.2. SEM images of CoCrWMo powders in different particle size distribution. (a)(b) S1, (c)(d) S2, (e)(f) S3, (g)(h) S4, (i)(j) S5, (k)(l) S6.

The particle size distribution (PSD) plots were obtained from 3D (diameter of the spheres) values. Figure 4.3. represents the PSD plots of S1, S2, S3, S4, S5, and S6 samples. The average size was calculated 31.27±9.46 µm, 34.30±6.97 µm, 58.72±7.08 µm, 19.04±10.91 µm, 18.54±7.05, µm and 55.0±5.75 µm respectively by using Image J. The D50 values of samples was calculated, 27.71 µm, 32.02 µm, 49.92 µm, 18.26 µm, 14.94 µm, and 45.20 µm respectively by using laser diffraction method. Two different measurement methods verify the mean particle size of the samples.

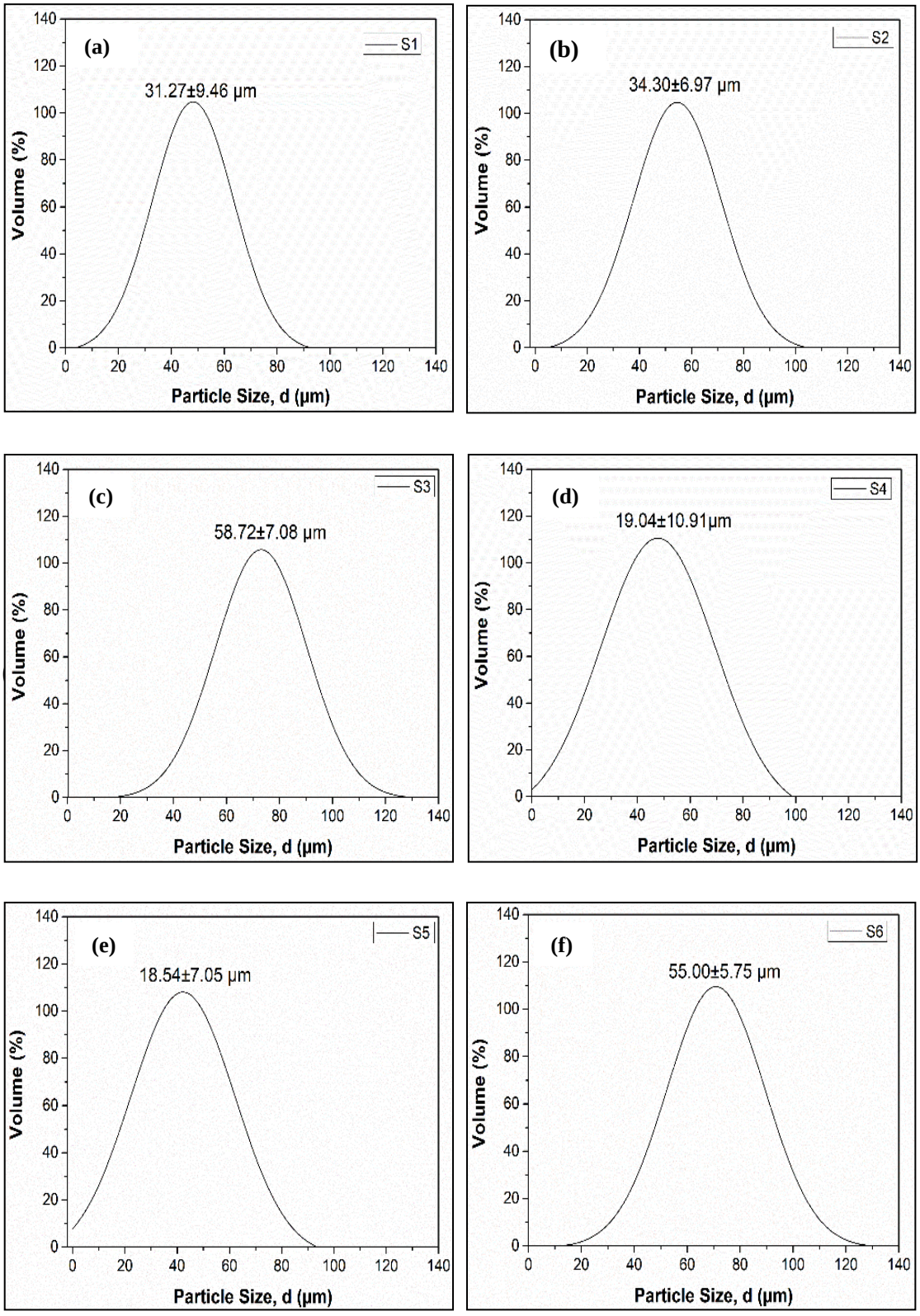

Figure 4.3. The Particle size distribution (PSD) plots of the samples (a) S1 (b) S2 (c) S3 (d) S4 (e) S5 (f) S6.

The AOR (α) is related to where is the height, is the diameter of the formed triangle is formulated as follows:

$$\alpha = \tan^{-1}\left(\frac{2H}{D}\right) \quad (4.1)$$

Figure 4.4. shows the AOR measurements of S3 and S5. S5 is a quiet cohesive powder due to the high fine particle content (particles below 20 µm is 66.58 % by volume), AOR result is 32.85º. S3 is the flowable powder (particles below 20 µm is 0 % by volume) AOR result is 21.33º. As expected, decreasing in flow rate (s/50g) results in lower AOR.[36]

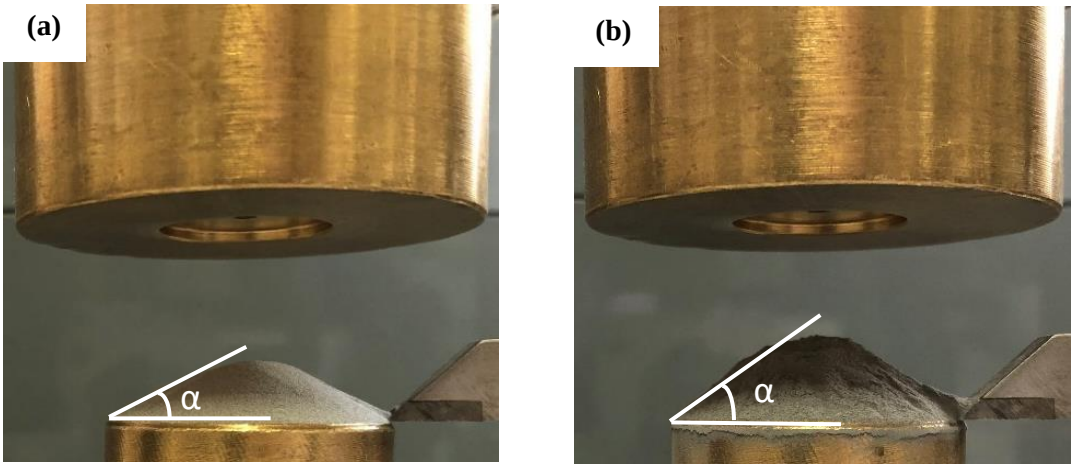

Figure 4.4. The angle of repose measurements of S3 and S5.

Apparent density, tap density, and flow rate results are tabulated in Table 4.2. A flow rate of the S4 and S5 were not quantified due to include a high amount of fine powders. The lowest flow rate and AOR values were measured as 14.19 s/50g and 4.86 g/cm^3 in S3. The highest apparent density measured as 5.02 g/cm3 in S4 and the lowest apparent density measured 4.78 g/cm^3 in S1. While D_{90} values of the S1 and S4 were measured as approximately 44 µm, particles below the 10 µm were recorded as 0% and 18.26% by volume. That causes the different apparent density values because fine particles fill into coarse particles' gaps and increase the apparent density.

Table 4.2. Powder characterization results of the samples S1, S2, S3, S4, S5, S6. (- indicates no flow is obtained). Average results were given after five consistent measurements.

Sample Code	S1	S2	S3	S4	S5	S6
Apparent Density (g/cm^3)	4.78	4.80	4.86	5.02	4.97	4.81
Tap Density (g/cm^3)	5.29	4.96	5.23	5.65	5.55	5.12
Flow Rate (s/50 g)	15.08	14.35	14.19	-	-	15.30
Angle of Repose (^{o})	22.39	22.01	21.33	26.97	32.85	20.65

Impurity content (C, S, O, N, Ar) of the metal powders is significant for the characterization of metal powders. A decrease in particle size results in an increase of oxygen content due to higher surface area. S5 includes the highest oxygen content comparing to others, due to the high fine metal powder ratio. An increase in oxygen amount can be induced by a change in melting temperature and a change in reflectivity/absorptivity properties of the powder.

Table 4.2.1. Oxygen amount results of the samples measured with hot gas extraction method.

Sample Code	S1	S2	S3	S4	S5	S6
Oxygen Amount (ppm)	246	241	207	347	384	243
Oxygen Amount (wt.%)	0.02	0.02	0.02	0.03	0.03	0.02

4.1. Spreadability Results Determined by Image Processing

Spreadabilitiy of the first, second, and third layers of the powder samples coded as S1, S2, S3, S4, S5 and S6 were processed from taken images with MATLAB. Firstly, the image cropped as a circle from the raw image, then edge detection and threshold applied to the cropped image. The black to white ratio was determined by the threshold image. This ratio is specified to determine the defects on the spread powder layer, and it is used for correlating the existing powder characterization methods. All measurements were conducted according to the MATLAB image processing algorithm. The results of measurements are given in Table 4.4.

As seen in Figure 4.5, any irregularity on the powder bed was not seen in layer 1, layer 2, and layer 3 of the spread S1. An average grayscale value of layer 1, layer 2, and layer 3 were quantified higher than 95 as 119.84, 115.96, and 135.05, respectively, and calculated from cropped raw images (see Figure 4.5. a, b, c). The average black to white ratio of layer 1, layer 2, and layer 3 was measured lower than 0.32 as 0.31, 0.30, and 0.21, respectively (see Figure 4.5. g, h, i). Besides, S1 is a flowable powder (it can be seen from the results of flow rate and AOR were measured as 15.08 s/50 g, 22.39^{o}) and so that homogeneous powder layers were recorded.

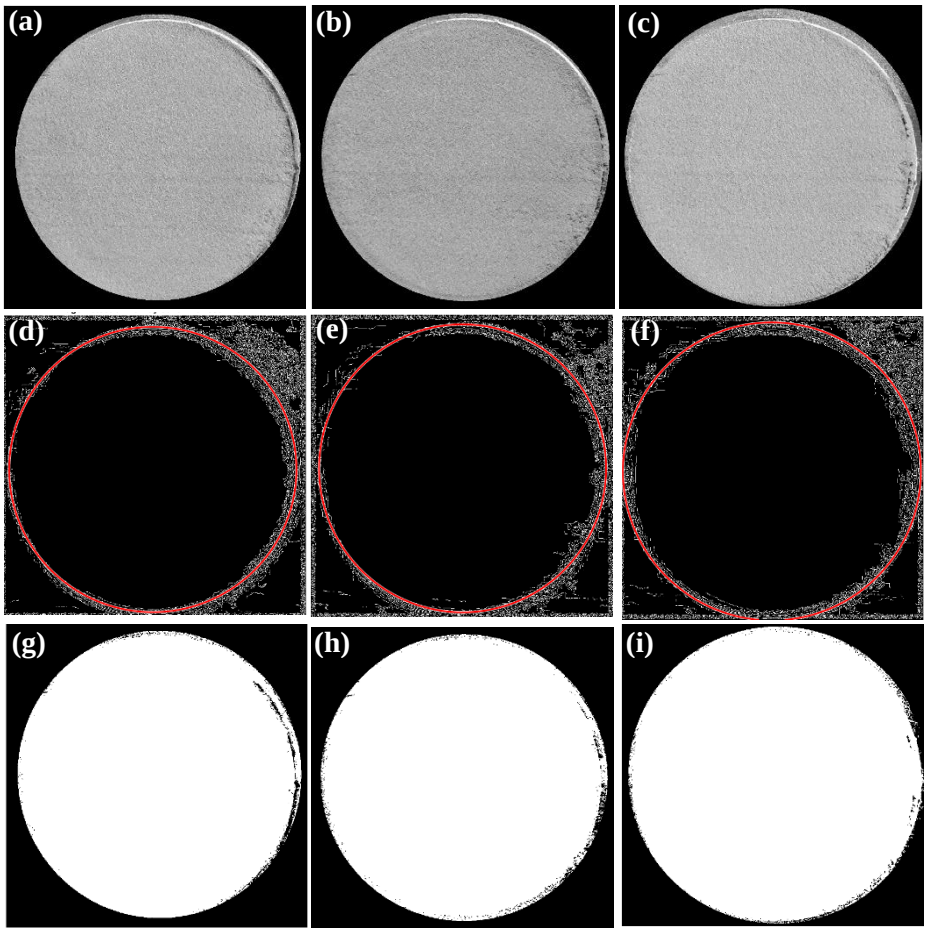

Figure 4.5. Cropped raw images of spread layers of S1 (a) layer 1 (b) layer 2 (c) layer 3. Edge detection applied layer images of S1 (d) layer 1 (e) layer 2 and (f) layer 3. Threshold applied layer images of S1 (g) layer 1 (h) layer 2 (e) layer 3.

As seen in Figure 4.6, some noises on the edge detection applied layer images were seen in layer 1, layer 2, and layer 3 of the spread S2. An average grayscale value of layer 1, layer 2, and layer 3 quantified higher than 95 as 107.04, 107.38, and 107.33,

respectively, and calculated from cropped raw images (see Figure 4.6. a, b, c). The average black to white ratio of layer 1, layer 2, and layer 3 measured as 0.31, 0.32, and 0.31, respectively (see Figure 4.6. g, h, i). Also, S2 is a flowable powder like S1, but the flowability is higher than S1 (it can be seen from the results of flow rate and AOR were measured as 14.35 s/50 g, 22.01^{o}), due to the mean particle size (D_{50}) is coarser 4.31 µm than S1, and homogeneous powder layers were recorded.

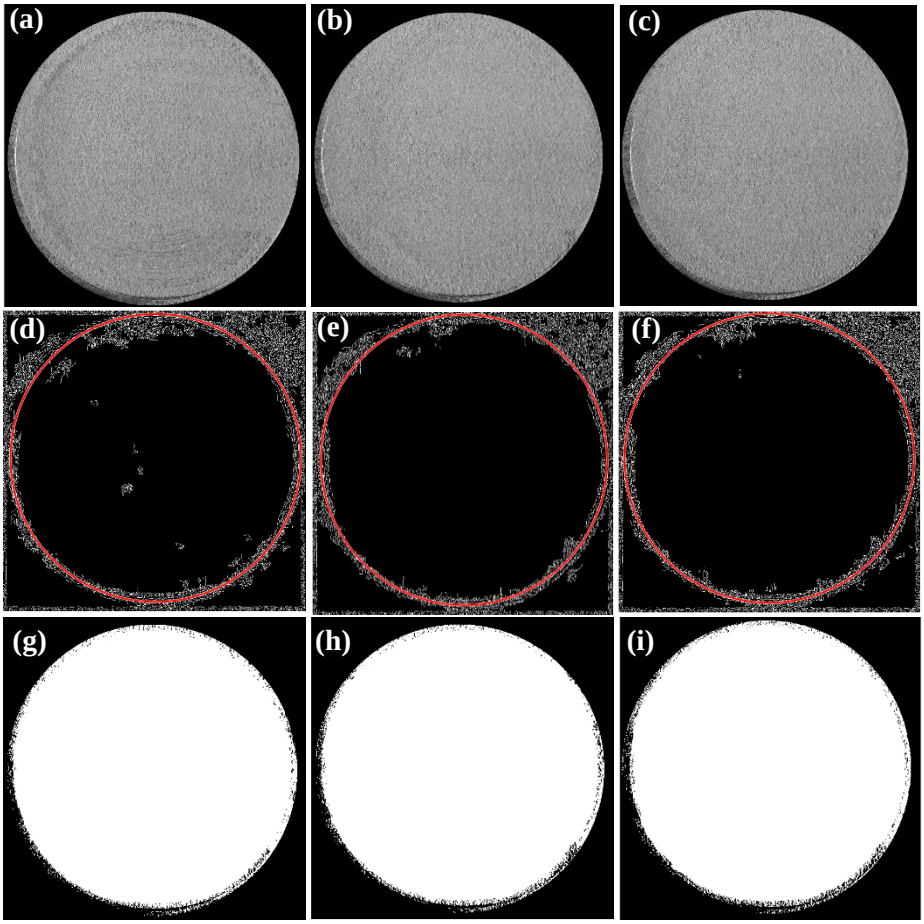

Figure 4.6. Cropped raw images of spread layers of S2 (a) layer 1 (b) layer 2 (c) layer 3. Edge detection applied layer images of S2 (d) layer 1 (e) layer 2 and (f) layer 3. Threshold applied layer images of S2 (g) layer 1 (h) layer 2 (e) layer 3.

As seen in Figure 4.7, irregularities on the powder bed were seen both cropped raw images, edge detection applied images, and threshold applied in layer 1 of the spread S3. Besides, S3 is the most flowable powder in all powder samples (it can be seen from the results of flow rate and AOR were measured as 14.19 s/50 g, 21.33^{o}). High

flowability may have caused the inadequate filling in layer 1. However, irregularities were not seen in layer 2 and layer 3 of the spread S3. The average grayscale values of layer 1, layer 2, and layer 3 quantified as 82.38, 113.67, and 115.09, which were calculated by cropped raw images Figure 4.7. a, b, c). The average black to white ratio of layer 1, layer 2, and layer 3 was conducted 0.60, 0.30, and 0.30 respectively calculated from the threshold image (see Figure 4.7. g, h, i).

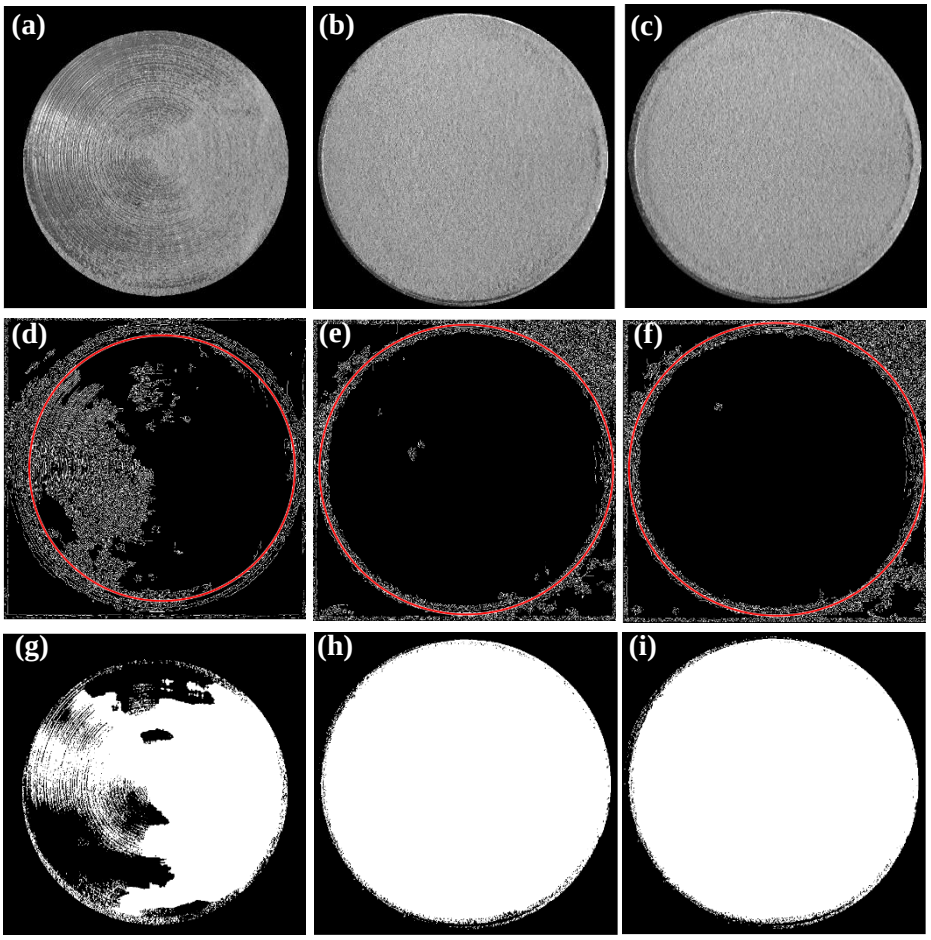

Figure 4.7. Cropped raw images of spread layers of S3 (a) layer 1 (b) layer 2 (c) layer 3. Edge detection applied layer images of S3 (d) layer 1 (e) layer 2 and (f) layer 3. Threshold applied layer images of S3 (g) layer 1 (h) layer 2 (e) layer 3.

The flow rate of S4 was not recorded, and it was seen as non-flowable visually. So that, irregularities on powder bed were seen clearly from the raw and edge detection applied images in layer 1, layer 2, and layer 3 of spread S4. However, these irregularities were not seen in threshold images. The reason is that the average grayscale value of

layer 1, layer 2, and layer 3 conducted higher than 95 as 109.45, 107.86, and 110.35 respectively calculated from cropped raw images (see Figure 4.8. a, b, c). Average black to white ratio of layer 1, layer 2, and layer 3 conducted as 0.30, 0.31, and 0.30 respectively calculated from threshold image (see Figure 4.8. g, h, i).

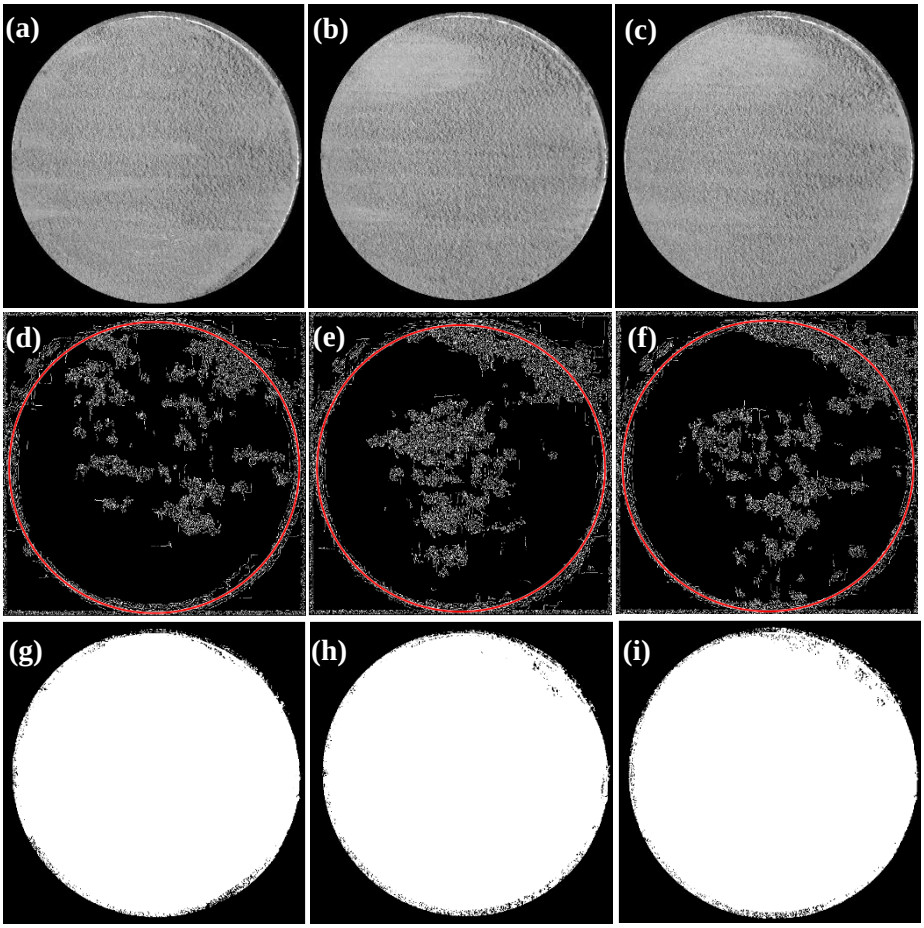

Figure 4.8. Cropped raw images of spread layers of S4 (a) layer 1 (b) layer 2 (c) layer 3. Edge detection applied layer images of S4 (d) layer 1 (e) layer 2 and (f) layer 3. Threshold applied layer images of S4 (g) layer 1 (h) layer 2 (e) layer 3.

Irregularities on the powder bed were seen clearly from the raw and edge detection applied and threshold applied images in layer 1, layer 2, and layer 3 of spread S5. The reason is that S5 is the very cohesive powder and the AOR is highest in all powder samples measured as 32.85^{o} and the flow rate value was not recorded like S4. An average grayscale value of layer 1, layer 2, and layer 3 quantified lower than 95 as 94.49, 91.98, and 92.66 respectively, calculated from cropped raw images (see Figure 4.9. a, b, c). The average black to white ratio of layer 1, layer 2, and layer 3 measured

higher than 0.32 as 0.37, 0.40, and 0.46 respectively calculated from the threshold image (see Figure 4.9. g, h, i).

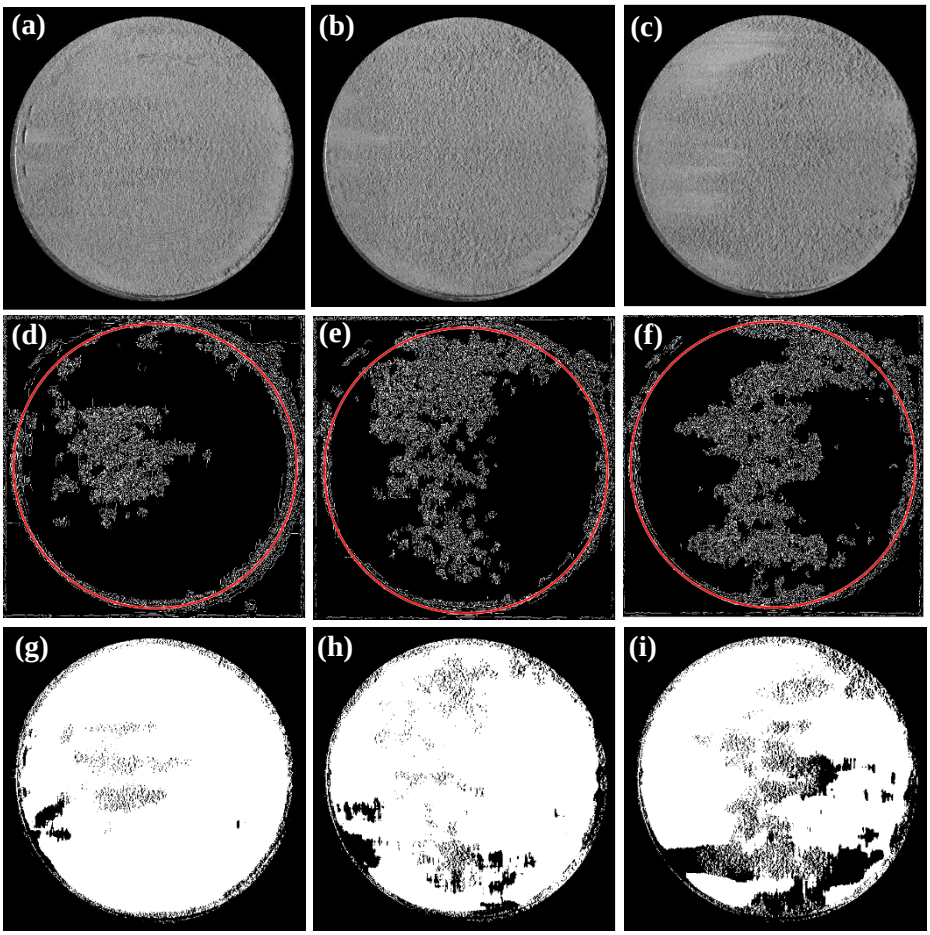

Figure 4.9. Cropped raw images of spread layers of S5 (a) layer 1 (b) layer 2 (c) layer 3. Edge detection applied layer images of S5 (d) layer 1 (e) layer 2 and (f) layer 3. Threshold applied layer images of S5 (g) layer 1 (h) layer 2 (e) layer 3.

According to the image processing results, irregularities on the powder bed were seen both cropped raw, edge detection applied, and threshold applied images in layer 1 of the spread S6. This is due probably to high flowability, may have caused the layer 1 to not fill. However, irregularities were not seen in layer 2 and layer 3 of the spread S6. The average grayscale value of layer 1, layer 2, and layer 3 quantified as 87.28, 108.03, and 107.72, respectively calculated from cropped raw images (see Figure 4.10. a, b, c). The average black to white ratio of layer 1, layer 2, and layer 3 measured as 0.56, 0.34,

and 0.34, respectively calculated from the threshold image (see Figure 4.10. g, h, i). S6 showed similar spreadability like S3.

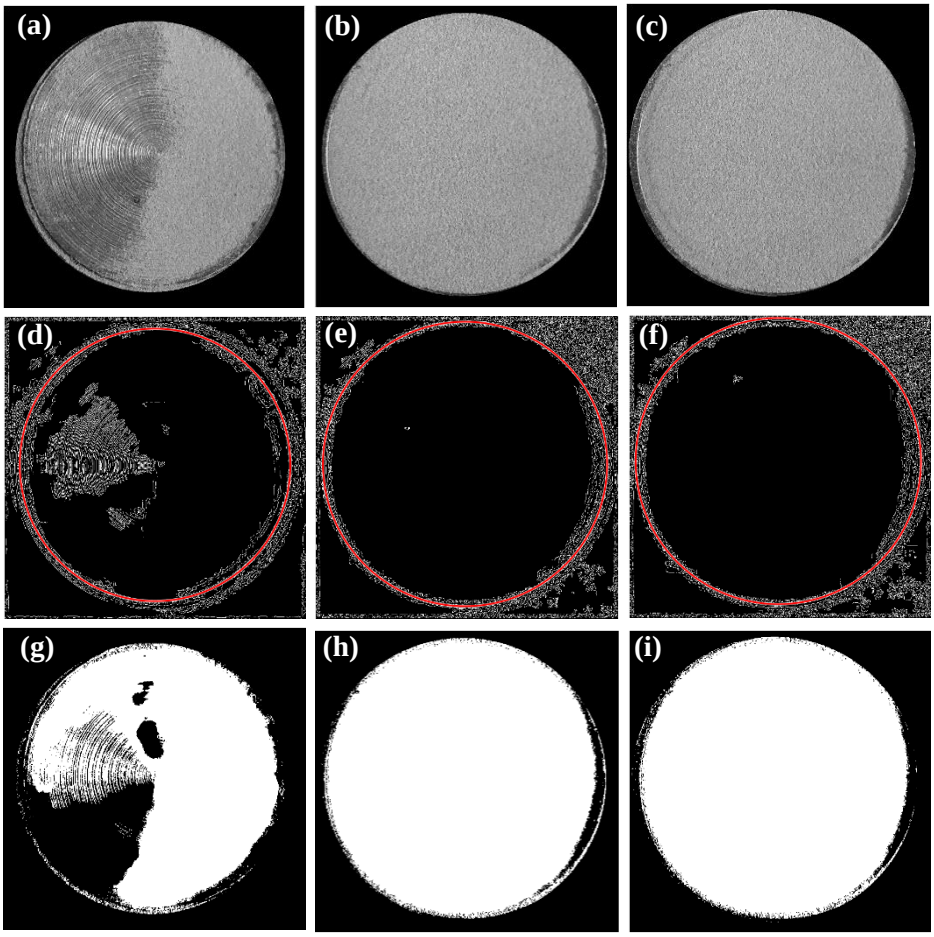

Figure 4.10. Cropped raw images of spread layers of S6 (a) layer 1 (b) layer 2 (c) layer 3. Edge detection applied layer images of S1 (d) layer 1 (e) layer 2 and (f) layer 3. Threshold applied layer images of S1 (g) layer 1 (h) layer 2 (e) layer

All spreadability tests were conducted with the constant spreading speed, which is 200 mm/s and the used blade material was rubber. In addition to the parameters that are used during this process, other studies suggest that there may be several parameters that affect the spreadability behavior of the powders such as different blade materials and different spreading speeds.[36]

Table 4.4. The average gray scale value (calculated from the cropped raw image) and black to white ratio (calculated from threshold image) of each layer after spreadability test performed by S1, S2, S3 and S5.

Sample Name	Average Grayscale Value (0 to 255)	Black to White Ratio
S1-Layer 1	119.84	0.31
S1-Layer 2	115.96	0.30
S1-Layer 3	135.05	0.26
S2-Layer 1	107.04	0.31
S2-Layer 2	107.38	0.32
S2-Layer 3	107.33	0.31
S3-Layer 1	82.38	0.60
S3-Layer 2	113.67	0.30
S3-Layer 3	115.09	0.30
S4-Layer 1	109.45	0.30
S4-Layer 2	107.86	0.31
S4-Layer 3	110.35	0.30
S5-Layer 1	94.49	0.37
S5-Layer 2	91.98	0.40
S5-Layer 3	92.66	0.46
S6-Layer 1	87.28	0.56
S6-Layer 2	108.03	0.34
S6-Layer 3	107.72	0.34

4.2. Porosity (%) Measurements of 3D Printed Cubes

While porous materials are an important class of materials[51,52], here the aim was to produce samples with highest relative density. According to spreadability test results, powder samples coded as S1, S2, S3, and S5 were chosen to determine the effects on final 3D printed cubes. The choice of these four samples depends on several reasons. Firstly, S1 and S2 showed similar spreadability behaviors, but comparing to S1, S2 involves slightly coarser particles. Secondly, S3 and S6 showed similar spreadability behaviors, but only S3 was chosen. Finally, S6 was chosen to show poor spreadability behavior comparing to the other five powder samples.

Two cubes were produced from each powder sample by L-PBF. After production, cubes were removed from the platform with wire erosion. In measurements, the cubes were named differently, such as S1-1 (first cube produced with S1) and S1-2

(second cube produced with S1). The side length of the cubes was 8 mm, but it decreases due to the wire erosion process of 1 mm.

Bulk density and porosity (%) measurements of the cubes produced by the L-PBF process are reported in Table 4.5. Calculated porosity (%) formulation is as follows:[26]

$$\%Porosiy = \left(1 - \frac{\rho_{measured}}{\rho_{true}}\right) \times 100 \quad (4.2)$$

Table 4.5. Bulk density (g/cm^3) and Porosity (%) measurement results of the cubes.

Sample Name	True Density (g/cm3) *	Bulk Density (g/cm^3) (Calculated from Geometrical Measurement)	Bulk Density(g/cm^3) (Calculated from Archimedes Measurement)	Porosity (%) (Calculated from Geometric Measurement)	Porosity (%) (Calculated from Archimedes Measurement)
S1-1	8.64±0.009	7.70±0.055	8.45±0.044	10.91±0.640	2.20±0.505
S1-2		7.70±0.043	8.40±0.058	10.99±0.503	2.78±0.671
S2-1		7.78±0.083	8.13±0.015	10.01±0.957	5.90±0.175
S2-2		7.70±0.063	8.28±0.008	10.95±0.729	4.17±0.054
S3-1		7.77±0.068	8.45±0.004	10.18±0.785	2.20±0.050
S3-2		7.62±0.045	8.44±0.057	11.89±0.522	2.31±0.666
S5-1		7.74±0.029	8.32±0.035	10.53±0.337	3.70±0.403
S5-2		7.83±0.050	8.40±0.020	9.43±0.580	2.78±0.232

*: True density was measured from the powder with He pycnometry.

As seen in the results, porosity amounts (%) are high for all produced cubes using S1, S2, S3, and S5, even S1(15-45 μm) that produced with commercially supplied powder show similarities with others. The fully dense part is crucial for AM, but the obtained values are not suitable for AM. Furthermore, differences in porosity measurements are determined for the first cube and second cube produced with each sample. Porosity amounts are between 8.85% and 12.41 calculated from geometric measurements and, the other is between 1.69% and 6.07% calculated from Archimedes measurements. This might be directly related to L-PBF process parameters (laser power, laser speed, layer thickness, oxygen rate during the production, etc.) During the production, spatter formation is obtained, and it can change the oxygen rate, PSD of the powder, and results in the pore formation.[26,41,53] From all samples, minimum porosity values are obtained in the cube 1 and cube 2, which are produced with S3. This may be

related to layer thickness. During the cube production, layer thickness was 50 μm and also the D50 of S3 was measured as 50 μm.

The upper and front surfaces of 3D printed cubes are shown in Figure 4.11. As seen, there are roughness on both upper and front surfaces. The reasons for surface roughness may be based on the production of cubes with different PSD and the process parameters.[44]

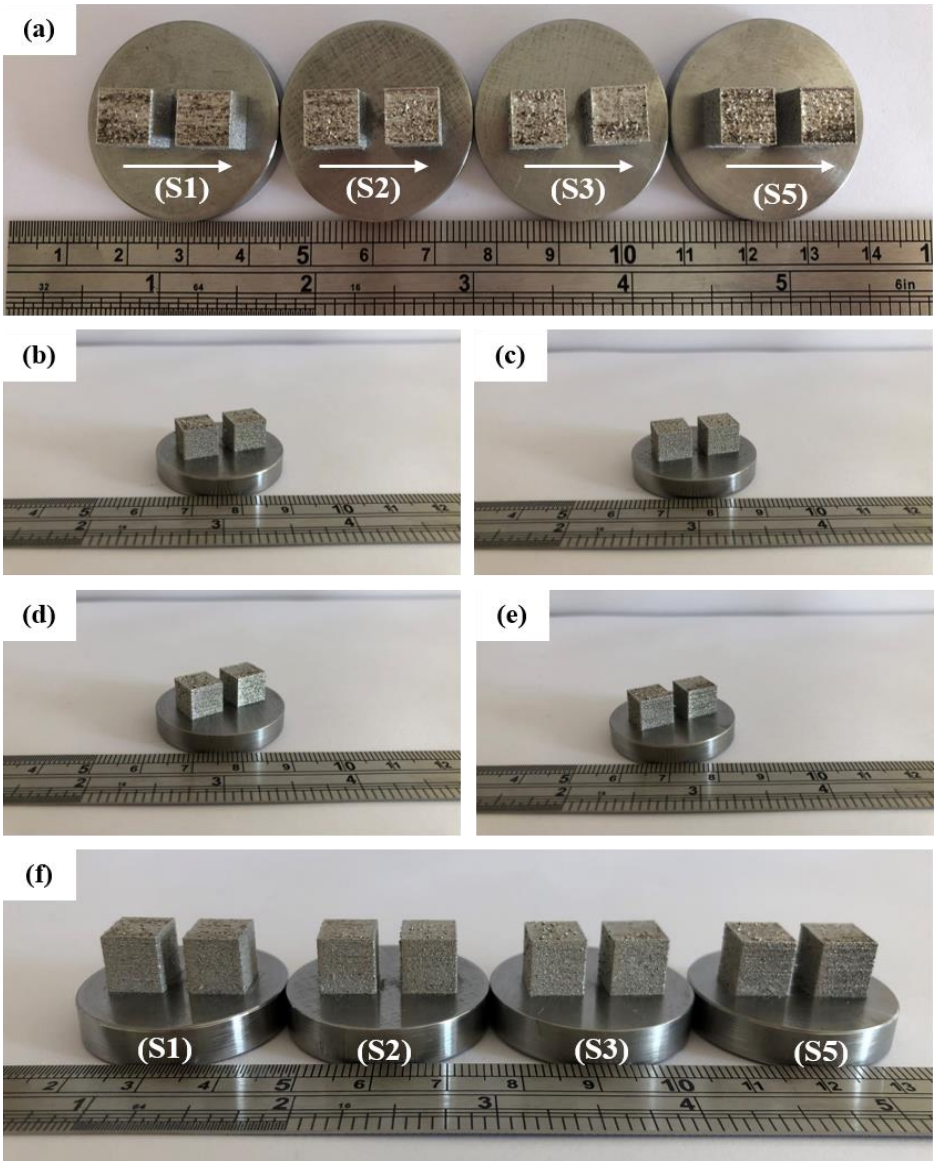

Figure 4.11. 3D printed cubes produced with Laser-Powder Bed Fusion Process. (a) Upper surface (f) front surface of the cubes produced by samples of S1, S2, S3 and S5 respectively. Cubes produced by (b) S1 (c) S2 (d) S3 (e) S5. Cube edge length 8 mm.

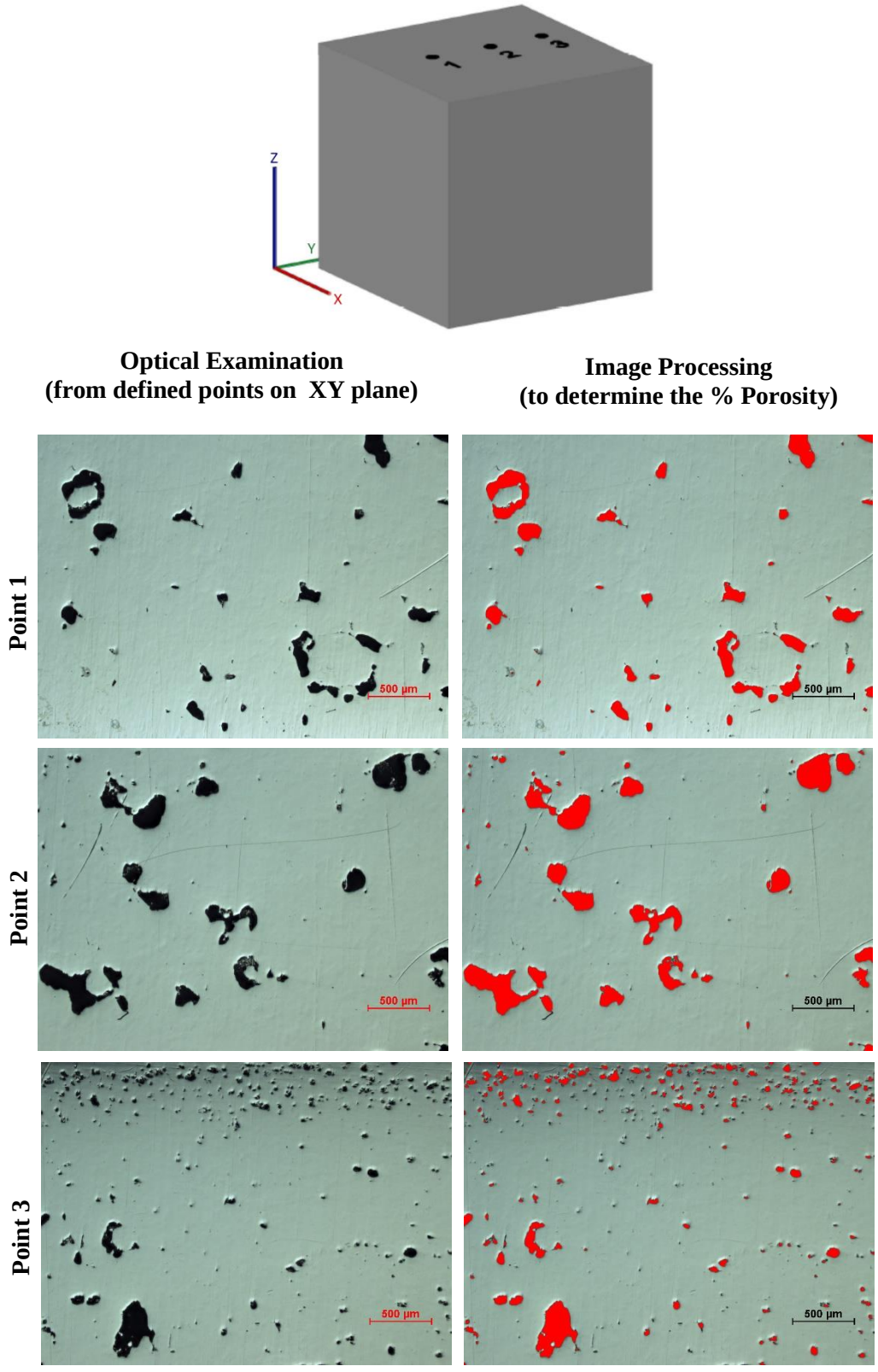

Figure 4.12. The optical microscope images of the cube S2-1 on XY plane, defined points 4, 5 and 6. (scale bar: 500 µm)

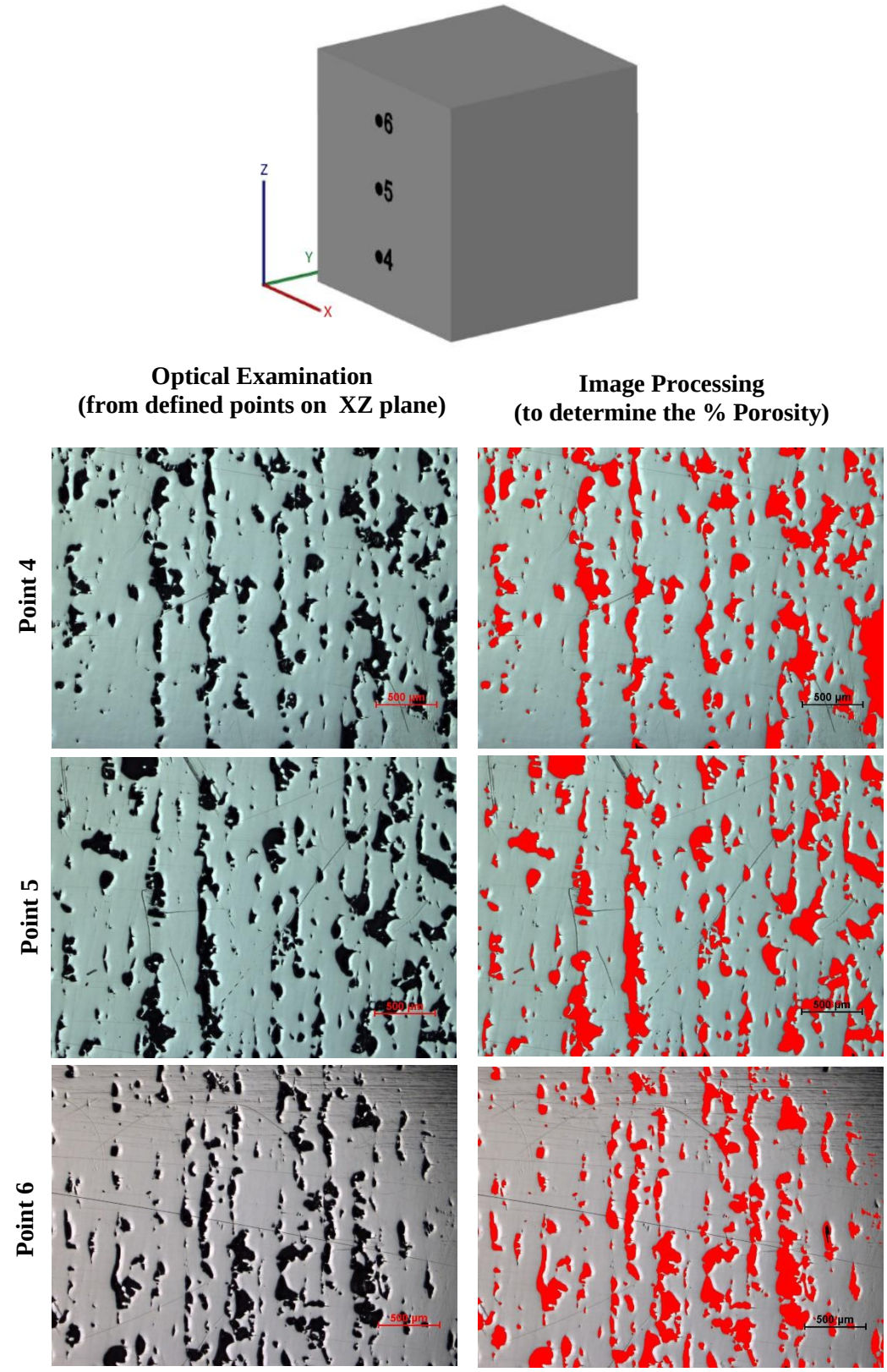

Figure 4.13. The optical microscope images of the cube S2-1 on XZ plane, defined points 4, 5 and 6. (scale bar: 500 µm)

Porosity measurements are also calculated from image processing as seen in Figure 4.12. and 4.13 and high porosity (%) also obtained defined points on both XY and XZ planes of the cube samples (see Table 4.6. and Table 4.7.). All porosity (%) measurements prove that process parameters are not suitable to observe the effects of spreadability on the final 3D printed parts.

Table 4.6. Porosity (%) results of the cubes calculated from defined points on XY planes via image processing.

Sample Name	Porosity (%) (Calculated from Image Processing)	Sample Name	Porosity (%) (Calculated from Image Processing)
S1-1-XY-1	12.91	**S3-1-XY-1**	3.58
S1-1-XY-2	6.09	**S3-1-XY-2**	0.80
S1-1-XY-3	2.53	**S3-1-XY-3**	2.85
S1-2-XY-1	8.74	**S3-2-XY-1**	6.28
S1-2-XY-2	6.88	**S3-2-XY-2**	8.82
S1-2-XY-3	5.09	**S3-2-XY-3**	11.12
S2-1-XY-1	4.06	**S5-1-XY-1**	6.54
S2-1-XY-2	6.17	**S5-1-XY-2**	11.35
S2-1-XY-3	3.18	**S5-1-XY-3**	4.86
S2-2-XY-1	3.40	**S5-2-XY-1**	2.20
S2-2-XY-2	4.16	**S5-2-XY-2**	2.42
S2-2-XY-3	4.40	**S5-2-XY-3**	5.82

Table 4.7. Porosity (%) results of the cubes calculated from defined points on XZ planes via image processing.

Sample Name	Porosity (%) (Calculated from Image Processing)	Sample Name	Porosity (%) (Calculated from Image Processing)
S1-1-XZ-4	10.13	**S3-1-XZ-4**	1.43
S1-1-XZ-5	24.06	**S3-1-XZ-5**	5.50
S1-1-XZ-6	25.94	**S3-1-XZ-6**	6.53
S1-2-XZ-4	6.11	**S3-2-XZ-4**	6.43
S1-2-XZ-5	8.24	**S3-2-XZ-5**	12.28
S1-2-XZ-6	6.56	**S3-2-XZ-6**	8.18
S2-1-XZ-4	17.75	**S5-1-XZ-4**	8.57
S2-1-XZ-5	18.26	**S5-1-XZ-5**	8.66
S2-1-XZ-6	17.38	**S5-1-XZ-6**	7.57
S2-2-XZ-4	11.06	**S5-2-XZ-4**	6.67
S2-2-XZ-5	22.54	**S5-2-XZ-5**	12.11
S2-2-XZ-6	26.91	**S5-2-XZ-6**	5.52

CHAPTER 5

CONCLUSIONS

According to our studies, powder spreadability can be analyzed quantitatively via image processing algorithms by using software such as MATLAB. According to the developed image processing algorithm, in average grayscale values (0 to 255) lower than 95 on cropped images, and black to a white ratio higher than 0.32 on threshold applied images, irregularities were observed. Such spreading irregularities can cause unwanted microstructural developments, or it can also deliberately be used to form porous components depending on the user requests.

It was observed that when the powder had a higher flowability, it caused a reduction in the angle of repose, as seen for the samples coded as S3 and S6, which showed inadequate spreadability. In addition, the increase in the amount of fine particles (e.g., below 10 μm) caused an agglomeration, decreased flowability, and an akin insufficient spreadability. For example, the S5 sample having the highest amount of particles sized <10 μm (%28.06) demonstrated to have an average grayscale value lower than 95, and black to a white ratio higher than 0.32. Therefore, flowability value should be neither too high nor too low, but the one allowing a coating with an optimum apparent density that seems to be affected by the particle size distribution, particle morphology, etc. is needed for better spreadability as seen for the samples S1 and S2.

Following the spreadibilty tests, comparable cubes with 8 mm edge length were produced with the L-PBF process to observe the effect of PSD on total porosity (%). While no mechanical tests were conducted, the samples were found to be porous and such porous structures might be related to the combination of various factors including poor spreadability, spatter formation, and other L-PBF processing parameters.

As shown in this thesis study that it is currently not an easy task to investigate the correlation between spreadability and standardized characterization techniques, and propose a method to quantify spreadability, and thus there is still a need for more detailed and statistical studies. For example, in the current work, spreadability tests for each sample conducted at constant spreading speed (200 mm/s) with continuous layer thickness (50 μm); the effects of spreading speed, layer thicknesses and their impact with varying powder characteristics on the final component morphology will be conducted in the future studies.

REFERENCES

1. ISO/ASTM 52900:2015: Additive manufacturing -- General principles -- Terminology (International Organization for Standardization, Geneva, Switzerland)

2. Tuncer, N.; Bose, A. Solid-State Metal Additive Manufacturing: A Review. *Jom* 2020.

3. Yasa, E. Understanding Adopting Selective Laser Melting of Metallic Materials. 2018, 1232–1245.

4. Zhang, W.; Mehta, A.; Desai, P. S.; Fred Higgs III, C. Machine Learning Enabled Powder Spreading Process Map for Metal Additive Manufacturing (AM). 2017, 1235–1249.

5. Krishnan, M.; Atzeni, E.; Canali, R.; Calignano, F.; Manfredi, D.; Ambrosio, E. P.; Iuliano, L. On the Effect of Process Parameters on Properties of AlSi10Mg Parts Produced by DMLS. *Rapid Prototyp. J.* 2014, *20* (6), 449–458.

6. Hoeges, S.; Zwiren, A.; Schade, C. Additive Manufacturing Using Water Atomized Steel Powders. *Met. Powder Rep.* 2017, *00* (00), 1–7.

7. Dawes, J.; Bowerman, R.; Trepleton, R. Introduction to the Additive Manufacturing Powder Metallurgy Supply Chain. *Johnson Matthey Technol. Rev.* 2015, *59* (3), 243–256.

8. Snow, Z. Understanding Powder Spreadability in Powder Bed Fusion. 2018, No. August, 1–143.

9. Neikov, O. D.; Stanislav S. Naboychenko. *Handbook of Non-Ferrous Metal Powders Technologies and Applications*; 2015; Vol. 3.

10. Gibson, I.; Rosen, D.; Stucker, B. *Additive Manufacturing Technologies: 3D Printing, Rapid Prototyping, and Direct Digital Manufacturing, Second Edition*; 2015.

11. Yang, L.; Hsu, K.; Baughman, B.; Godfrey, D.; Medina, F.; Menon, M.; Wiener, S. *Additive Manufacturing of Metals: The Technology, Materials, Design and Production*; 2017.

12. Anderson, I. E.; White, E. M. H.; Dehoff, R. Feedstock Powder Processing Research Needs for Additive Manufacturing Development. *Curr. Opin. Solid State Mater. Sci.* 2018, *22* (1), 8–15.

13. web1: https://www.carpenteradditive.com/Technical-Library. (Access date: 16.04.2020)

14. Mueller, B.; Hund, R.; Malek, R.; Gebauer, M.; Polster, S.; Kotzian, M.; Neugebauer, R. Added Value in Tooling for Sheet Metal Forming through Additive Manufacturing. *Int. Conf. Compet. Manuf.* 2013, No. January, 1–7.

15. Pleass, C.; Jothi, S. Influence of Powder Characteristics and Additive Manufacturing Process Parameters on the Microstructure and Mechanical Behaviour of Inconel 625 Fabricated by Selective Laser Melting. *Addit. Manuf.* 2018, *24* (May), 419–431.

16. Vock, S.; Klöden, B.; Kirchner, A.; Weißgärber, T.; Kieback, B. Powders for Powder Bed Fusion: A Review. *Prog. Addit. Manuf.* 2019, *4* (4), 383–397.

17. Li, R.; Shi, Y.; Wang, Z.; Wang, L.; Liu, J.; Jiang, W. Densification Behavior of Gas and Water Atomized 316L Stainless Steel Powder during Selective Laser Melting. *Appl. Surf. Sci.* 2010, *256* (13), 4350–4356.

18. ASTM International. Standard Test Method for Apparent Density of Free-Flowing Metal Powders Using The. 2013, *i*, 1–4.

19. Saw, H. Y.; Davies, C. E.; Paterson, A. H. J.; Jones, J. R. Correlation between Powder Flow Properties Measured by Shear Testing and Hausner Ratio. *Procedia Eng.* 2015, *102*, 218–225.

20. Nan, W.; Ghadiri, M.; Wang, Y. Analysis of Powder Rheometry of FT4: Effect of Particle Shape. *Chem. Eng. Sci.* 2017, *173*, 374–383.

21. Markusson, L. Powder Characterization for Additive Manufacturing Processes. 2017, 117.

22. Mostafaei, A.; Elliott, A. M.; Barnes, J. E.; Cramer, C. L.; Chmielus, M.; Elliott, A. M.; Barnes, J. E. Binder Jet 3D Printing; Process Parameters, Materials, Properties, and Challenges. *Prog. Mater. Sci.* 2020, 100684.

23. Geyer, F. Additive Manufacturing: Making Sense of Laser Metal Deposition and 3D Printing (web2: https://www.fabricatingandmetalworking.com/2016/07/additive-manufacturing- making-sense-laser-metal-deposition-3d-printing/). (Access date: 16.07.2020)

24. web3: https://www.additively.com/en/learn-about/3d-printing-technologies. (Access date:2.03.2020)

25. Spierings, A. B. Powder Spreadability and Characterization of Sc- and Zr-Modified Aluminium Alloys Processed by Selective Laser Melting Quality Management System for Additive Manufacturing. 2018.

26. Sola, A.; Nouri, A. Microstructural Porosity in Additive Manufacturing: The Formation and Detection of Pores in Metal Parts Fabricated by Powder Bed Fusion. *J. Adv. Manuf. Process.* 2019, *1* (3).

27. Gokuldoss, P. K.; Kolla, S.; Eckert, J. Additive Manufacturing Processes: Selective Laser Melting, Electron Beam Melting and Binder Jetting-Selection Guidelines. *Materials (Basel).* 2017, *10* (6).

28. Jadhav, S. D.; Dadbakhsh, S.; Goossens, L.; Kruth, J. P.; Van Humbeeck, J.; Vanmeensel, K. Influence of Selective Laser Melting Process Parameters on Texture Evolution in Pure Copper. *J. Mater. Process. Technol.* 2019, *270* (February), 47–58.

29. Aboulkhair, N. T.; Simonelli, M.; Parry, L.; Ashcroft, I.; Tuck, C.; Hague, R. 3D Printing of Aluminium Alloys: Additive Manufacturing of Aluminium Alloys Using Selective Laser Melting. *Prog. Mater. Sci.* 2019, *106* (July), 100578.

30. Yasa, E.; Kempen, K.; Kruth, J. .-; L., T.; Humbeeck, J. Microstructure And Mechanical Properties Of Maraging Steel 300 After Selective Laser Melting. 2010, *21*, 427–441.

31. Wei, W.; Zhou, Y.; Liu, W.; Li, N.; Yan, J.; Li, H. Microstructural Characterization, Mechanical Properties, and Corrosion Resistance of Dental Co-Cr-Mo-W Alloys Manufactured by Selective Laser Melting. *J. Mater. Eng. Perform.* 2018, *27* (10), 5312–5320.

32. Liu, S.; Shin, Y. C. Additive Manufacturing of Ti6Al4V Alloy: A Review. *Mater. Des.* 2019, *164*, 107552.

33. Bordin, A.; Ghiotti, A.; Bruschi, S.; Facchini, L.; Bucciotti, F. Machinability Characteristics of Wrought and EBM CoCrMo Alloys. *Procedia CIRP* 2014, *14*, 89–94.

34. Sun, S. H.; Koizumi, Y.; Saito, T.; Yamanaka, K.; Li, Y. P.; Cui, Y.; Chiba, A. Electron Beam Additive Manufacturing of Inconel 718 Alloy Rods: Impact of Build Direction on Microstructure and High-Temperature Tensile Properties. *Addit. Manuf.* 2018, *23* (August), 457–470.

35. Sun, Y. Y.; Gulizia, S.; Oh, C. H.; Doblin, C.; Yang, Y. F.; Qian, M. Manipulation and Characterization of a Novel Titanium Powder Precursor for Additive Manufacturing Applications. *Jom* 2015, *67* (3), 564–572.

36. Snow, Z.; Martukanitz, R.; Joshi, S. On the Development of Powder Spreadability Metrics and Feedstock Requirements for Powder Bed Fusion Additive Manufacturing. *Addit. Manuf.* 2019, *28*, 78–86.

37. Brika, S. E.; Letenneur, M.; Dion, C. A.; Brailovski, V. Influence of Particle Morphology and Size Distribution on the Powder Flowability and Laser Powder Bed Fusion Manufacturability of Ti-6Al-4V Alloy. *Addit. Manuf.* 2020, *31* (November), 100929.

38. Cordova, L.; Bor, T.; de Smit, M.; Campos, M.; Tinga, T. Measuring the Spreadability of Pre-Treated and Moisturized Powders for Laser Powder Bed Fusion. *Addit. Manuf.* 2020, *32* (April 2019).

39. Craeghs, T.; Stijn, C.; Evren, Y.; Jean-Pierre, K. Online Quality Control of Selective Laser Melting. *Office* 2011, *2* (3), 297.

40. Spierings, A. B.; Voegtlin, M.; Bauer, T.; Wegener, K. Powder Flowability Characterisation Methodology for Powder-Bed-Based Metal Additive Manufacturing. *Prog. Addit. Manuf.* 2016, *1* (1–2), 9–20.

41. Strondl, A.; Lyckfeldt, O.; Brodin, H.; Ackelid, U. Characterization and Control of Powder Properties for Additive Manufacturing. 2015, *67* (3), 549–554.

42. Condruz, M. R.; Matache, G.; Paraschiv, A. Characterization of IN 625 Recycled Metal Powder Used for Selective Laser Melting. 2020, *5*, 1–8.

43. Yablokova, G.; Speirs, M.; Van Humbeeck, J.; Kruth, J. P.; Schrooten, J.; Cloots, R.; Boschini, F.; Lumay, G.; Luyten, J. Rheological Behavior of β-Ti and NiTi Powders Produced by Atomization for SLM Production of Open Porous Orthopedic Implants. *Powder Technol.* 2015, *283*, 199–209.

44. Spierings, A. B.; Herres, N.; Levy, G. Influence of the Particle Size Distribution on Surface Quality and Mechanical Properties in AM Steel Parts. *Rapid Prototyp. J.* 2011, *17* (3), 195–202.

45. Chen, H.; Wei, Q.; Zhang, Y.; Chen, F.; Shi, Y.; Yan, W. Powder-Spreading Mechanisms in Powder-Bed-Based Additive Manufacturing: Experiments and Computational Modeling. *Acta Mater.* 2019, *179*, 158–171.

46. Nan, W.; Pasha, M.; Bonakdar, T.; Lopez, A.; Zafar, U.; Nadimi, S.; Ghadiri, M. Jamming during Particle Spreading in Additive Manufacturing. *Powder Technol.* 2018, *338*, 253–262.

47. Meier, C.; Weissbach, R.; Weinberg, J.; Wall, W. A.; John Hart, A. Modeling and Characterization of Cohesion in Fine Metal Powders with a Focus on Additive Manufacturing Process Simulations. *Powder Technol.* 2019, *343*, 855–866.

48. Ahmed, M.; Pasha, M.; Nan, W.; Ghadiri, M. A Simple Method for Assessing Powder Spreadability for Additive Manufacturing. *Powder Technol.* 2020, *367*, 671–679.

49. Vakifahmetoglu, C.; Balliana, M.; Colombo, P. Ceramic Foams and Micro-Beads from Emulsions of a Preceramic Polymer. *J. Eur. Ceram. Soc.* 2011, *31* (8), 1481–1490.

50. ASTM D3576 Standard Test Method for Cell Size of Rigid Cellular Plastics; 2015; Vol. 08.02.

51. Lefebvre, B. L.; Banhart, J.; Dunand, D. C. Porous Metals and Metallic Foams : Current Status and Recent Developments **. 2008, No. 9, 775–787.

52. Vakifahmetoglu, C.; Soraru, G. D. Closed Porosity Ceramics and Glasses. 2020, No. August 2019, 2941–2969.

53. Kim, F. H.; Moylan, S. P.; Garboczi, E. J.; Slotwinski, J. A. Investigation of Pore Structure in Cobalt Chrome Additively Manufactured Parts Using X-Ray Computed Tomography and Three-Dimensional Image Analysis. *Addit. Manuf.* 2017, *17*, 23–38.